Check for updates

International Journal for Numerical and Analytical Methods in Geomechanics

WILEY

RESEARCH ARTICLE OPEN ACCESS

Computational Analysis of the Vibrational Response of Lunar Regolith Made of Nonspherical Grains

Lewis Traquair[1] | Peter Watson[1] | Ali Anwar[1] | Sebastien Vincent Bonnieu[2] | Marcello Lappa[1]

[1]Department of Mechanical and Aerospace Engineering, University of Strathclyde, Glasgow, Scotland, UK | [2]European Space Agency, European Space Research and Technology Center, Noordwijk, the Netherlands

Correspondence: Marcello Lappa (marcello.lappa@strath.ac.uk)

Received: 29 January 2026 | **Revised:** 24 July 2026 | **Accepted:** 13 August 2026

Keywords: discrete element method | fluidization | granular material | mass flow | regolith | vibration

ABSTRACT

Vibration-based systems have shown that appropriately oriented and tuned mechanical oscillations can disrupt regolith interlocking and promote flow. Building on this evidence, the present study investigates vibration-controlled granular discharge as a potential ISRU (In Situ Resource Utilization) strategy, with the aim of supporting predictable material processing through physically consistent numerical modeling. The equations governing the dynamics of nonspherical particles are presented accordingly and used to simulate the behavior of a fixed mass of granular material flowing through a hopper device in the framework of the discrete element method (DEM). The results show that even for monodisperse distributions vibration-induced fluidization does not follow simple monotonic trends. The mass flow rate initially increases with the forcing frequency f, reaching a plateau in the range of 150–200 Hz, beyond which further frequency increases produce no significant enhancement. At the same time, higher values of the dimensionless acceleration Γ generally reduce the mass flow rate and cause an increase in the frequency threshold above which vibration-driven discharge exceeds gravity-driven flow. Moreover, for fixed, moderately low values of Γ, increasing f leads to the emergence of higher-order harmonics in the instantaneous mass flow rate. For fixed and relatively high values of f, a larger value of Γ can cause the appearance of subharmonics in the spectrum. In contrast, for relatively low f and high Γ, incommensurate spectral components appear, which reduce the regularity and predictability of the flow response. These findings are supported by a detailed analysis of particle patterning behavior and frequency spectra, which reveals the fine-scale dynamics underlying the observed flow regimes.

1 | Introduction

From the Apollo 11 to the recent launch of China's Chang'e 6 Lunar sampler and as witnesses by the more recent Artemis missions, a long-lasting interest exists in establishing a human presence on the Moon. Position papers such as the European Space Agencies "ESA Strategy for Science at the Moon" [1] have clearly identified and proposed missions to our satellite for purposes such as geophysics, material sampling, physical chemistry, examining ice caps at the lunar poles as sources of water, and monitoring of physiological effects of the lunar environment, just to cite a few examples. More recently, additional interest has been driven by the intention to exploit the Moon for the implementation of the so-called In Situ Resource Utilization (ISRU) strategy [2–4], for which the "Lunar regolith" is nowadays almost universally regarded as a key "factor."

Lunar regolith is defined as the layers of unconsolidated rock debris and granular material which cover the surface of the Moon, formed by ancient geological processes, impacts of its

This is an open access article under the terms of the Creative Commons Attribution License, which permits use, distribution and reproduction in any medium, provided the original work is properly cited.
© 2026 The Author(s). *International Journal for Numerical and Analytical Methods in Geomechanics* published by John Wiley & Sons Ltd.

surface with small solar system bodies and charged particles from the sun [5]. Depending on the location on the lunar surface, the regolith can reach up to 12 meters deep, such as in highland areas for example [6].

For future space missions aiming to create a stable presence on our satellite, transporting products from the Earth would be a financial and logistical burden. Hence, using materials in-situ is currently regarded as the most logical and sustainable way to acquire the needed resource whether it be for an autonomous or direct human presence [7–9]. As an example, one of the most obvious uses involves exploiting lunar soil to support the creation of long-term human habitats. From partially processed regolith, a range of construction materials can be produced, including so-called lunar concrete, prepared by combining lunar soil with hydraulic binders or other additives, as well as fiberglass and different types of glass-ceramic composites. Beyond its role as a raw material for additive manufacturing and three-dimensional printing, which could enable the fabrication of buildings and crewed infrastructure directly on the lunar surface, regolith is also viewed as a valuable reservoir of metals and other technologically relevant elements. Since sustained exploration and settlement will also require local food production, ongoing research is examining the use of lunar soil as a solid growth medium for plants and as a support environment for microbial communities involved in recycling and waste treatment.

A total of 382 kg of genuine lunar regolith was originally brought back by the Apollo missions [10]. The distribution of its particle size was characterized by Heiken et al. [11] and Connolly and Carrier [12]. These authors found that approximately 90% of the regolith particles were distributed between 1.33 mm and 3.3 nm in diameter, with the mean diameter being 72 μm, making it comparable to fine sand. Nevertheless, the observed frictional properties were very different from common terrestrial soil.

A comprehensive discussion of the issues involved with handling this material and related processing on the Moon can be found in the book by Walton [13], where the design of transportive or conveyance systems like bins or hoppers was used to demonstrate the unique requirements for systems which can initiate flow from these devices.

As highlighted in that book, there are numerous techniques used in industry, which could be theoretically modified and applied for use in lunar ISRU. These concern the agriculture field [14], pharmaceuticals [15], materials handling [16], mining [17], food processing [18], construction [19], power generation [20], and waste management [21]. Related methods used to manipulate granular materials generally rely on gravity [22], vibration-induced mixing [23] and aerodynamic segregation [24].

However, a simple extension of such concepts to the ISRU framework is made difficult or it is completely impeded by the fact that lunar regolith does not behave as a standard terrestrial material, because its grains are extremely angular and abrasive as a consequence of their formation by impact fragmentation and the absence of atmospheric, chemical, or hydrological agents that on Earth progressively smooth and round mineral particles.

As an example, Lee [25] discussed that the irregular geometry of regolith particles can lead to "mechanical interlocking" which aids the intrinsically adhesive nature of this material. Since then, many other authors have emphasized the extremely frictional nature of lunar regolith and the impossibility of managing it through standard (terrestrial) processes. Additionally, measurements and observations from the Surveyor, Apollo, and Luna missions demonstrated that lunar soil possesses cohesiveness also because of the near-vacuum conditions on the Moon, which eliminate the gas adsorption layers that, on Earth, surround soil grains and reduce friction by acting as a lubricating film ([26]; see also [27]).

Other bottlenecks preventing the application of terrestrial technologies stem from the nature of the lunar environment itself, where the absence of an atmosphere (no gases to implement pneumatic conveying systems) and the harsh temperature variations (often not compatible with complex mechanical systems and parts) further constrain the viable technical solutions.

However, over the last four or five years, a promising direction of research has been identified, which completely relies on the meaningful and rational utilization of *vibrational mechanical stimuli* to overcome many of the limitations set by lunar regolith and its environment.

Specifically, vibrating systems and related prototypes, such as those presented by Kawamoto [28] and Lappa et al. [29] have demonstrated that imposed vibrations of given direction, frequency and amplitude, can break apart the interlocking behavior of the regolith and cause it to flow [30–33].

Such findings build on a long-lasting line of inquiry that has traditionally dealt with monodisperse granular materials, generally comprising spherical particles. The ability of vibrations to alter the state of these collections of particles stems from a well-known concept. Granular materials constitute a paradigmatic class of athermal systems, for which the principles of classical thermodynamics are not applicable because the thermal energy is negligible compared with the gravitational potential energy associated with macroscopic particles. Consequently, a static granular assembly typically resides in a metastable state, effectively confined within a local minimum of the system's potential energy landscape. Upon exposure to external mechanical excitation, the packing receives an instantaneous input of mechanical energy that enables it to escape its current energy basin and evolve toward a new metastable configuration [34, 35]. The resulting state is determined not only by the characteristics of the applied perturbation but also by the history and structure of the preceding configuration [36, 37].

Given these theoretical premises, in this study, we concentrate on lunar-regolith vibration-controlled flow as a possible strategy to support the ISRU. More specifically, our objective originates from a relatively simple realization, that is, the processing of granular material requires *predictable operation* [22]. For this to be true, systems must be designed around the mechanical properties and expected behavior of the considered material; and in turn, to allow for such a design, adequate mathematical models and simulation capabilities must be made available.

Regardless of their terrestrial or extra-terrestrial origin, granular materials are generally comprised of many distinct particles which interact both with each other and with the boundary that contains them. Thus, both the inter-particle collisions and boundary interactions contribute to the system response. Numerical modeling is common practice to investigate such behaviors for engineering problems where the analytical predictions or models are highly complex. However, as explained above, lunar regolith does not behave as common terrestrial sand. Therefore, this requires the implementation and testing of new relevant models.

Since the discrete element method (DEM) is the numerical technique primarily used in the literature to predict the dynamics of lunar regolith [38–48], it is used in this study as well.

This study aims to address an important need aligned with the arguments above, that is, creating a *framework of increasing numerical accuracy for the simulations of lunar regolith subjected to vibrations* flowing through a hopper. Particular attention is devoted to the role of particle shape. Although the dynamics of vibrated granular systems have been extensively investigated in the literature, most existing numerical studies rely on spherical particles or simplified shape representations. By contrast, the response of lunar regolith under vibrational forcing conditions, modeled using explicitly nonspherical particles, remains largely unexplored. Given the highly angular morphology of lunar grains and the resulting interlocking and rotational constraints, particle shape is expected to play a significant role in determining pattern formation, energy dissipation, frequency response, and the emergence of collective dynamical behaviors. Accordingly, the present work constitutes a first step toward the systematic investigation of these effects through the use of polyhedral particles.

2 | The System

2.1 | Vibrational Effects

Vibrational excitation is applied to promote material flow and mitigate jamming at the hopper outlet. Excitation is imposed globally on the entire hopper rather than through localized devices, reflecting configurations commonly examined in the literature [28]. The imposed motion is sinusoidal and vertical, with frequency and amplitude treated as control parameters. This setup isolates the influence of vibration characteristics on regolith discharge behavior and blockage prevention.

Among the many physical quantities involved, we pay particular attention to the dimensionless acceleration Γ and the mass discharge rate W, both of which are widely used indicators of granular flow performance under vibration. These quantities are monitored as functions of vibration amplitude and frequency to identify thresholds beyond which additional excitation produces diminishing returns, or conditions under which shaking suppresses rather than enhances flow. Simulation results are compared with gravity-driven flow (no imposed vibrations) cases and with configurations involving alternative vibration orientations reported in the literature, allowing the specific role of vertical excitation to be quantified.

From a purely mathematical standpoint, vibrations are incorporated by imposing a time-periodic displacement on the physical boundary of the particle container:

$$\underline{s}^{vibr} = b\sin(\Omega\tau)\underline{\widehat{\kappa}} \tag{1}$$

where τ is the time, b and Ω are the amplitude and angular frequency of the vibrations ($\Omega = 2\pi f$), respectively, and $\underline{\widehat{\kappa}}$ is the unit vector along the shaking direction. Consequently, in a reference frame attached to the particle container, an acceleration is generated, which can be expressed as

$$\underline{a}(\tau) = \underline{g} - b\Omega^2\sin(\Omega\tau)\underline{\widehat{\kappa}} \tag{2}$$

where g is the gravity (steady) acceleration while $b\Omega^2$ results from the second derivative of the displacement function with respect to time. This indicates that in the container's reference frame, vibrations manifest as a time-varying acceleration with an amplitude determined by the product of b and the square of the angular frequency. By averaging the total acceleration acting on the particles in time, one gets

$$\begin{aligned}
\underline{a}_{average} &= \frac{\Omega}{2\pi}\int_0^{2\pi/\Omega}\underline{a}(\tau)d\tau \\
&= \frac{\Omega}{2\pi}\int_0^{2\pi/\Omega}\underline{g}d\tau - \frac{\Omega}{2\pi}\int_0^{2\pi/\omega} b\Omega^2\sin(\Omega\tau)\underline{\widehat{\kappa}}d\tau \\
&= \frac{\Omega}{2\pi}\underline{g}\int_0^{2\pi/\Omega} d\tau - \frac{\Omega}{2\pi}b\Omega^2\underline{\widehat{\kappa}}\int_0^{2\pi/\omega}\sin(\Omega\tau)\,d\tau \\
&= \underline{g} + \frac{1}{2\pi}b\Omega^2\underline{\widehat{\kappa}}[\cos(\Omega\tau)]_0^{2\pi/\Omega} = \underline{g}
\end{aligned} \tag{3}$$

The major importance of Equation (3) resides in its ability to demonstrate that vibrations do not contribute to any time-averaged acceleration or force, as shown mathematically by [36].

The aforementioned parameter Γ is introduced as:

$$\Gamma = \frac{b\Omega^2}{g} \tag{4}$$

It simply accounts for the relative importance of vibrational and gravitational inertial effects (in this study we assume $g = 9.81$ m/s^2).

Moreover, we define the mass flow rate as the total (initial) mass within the system (0.052 g) divided by the time to discharge. Finally, we introduce a dimensionless discharge rate W_d, which is found by dividing the mass flow rate under vibration by the mass flow rate under purely gravitational discharge.

2.2 | Hopper

The bounding dimensions of the hopper shown in Figure 1 are $16 \times 26 \times 1$ mm.

Within the hopper, a rectangular surface referred to as a "stopper" or "plug" (dark grey, Figure 1) was placed. The purpose of the stopper was to allow the inflowing particle matter to settle in the upper portion of the hopper before the applied vibrations would commence. As the material was settled (configuration

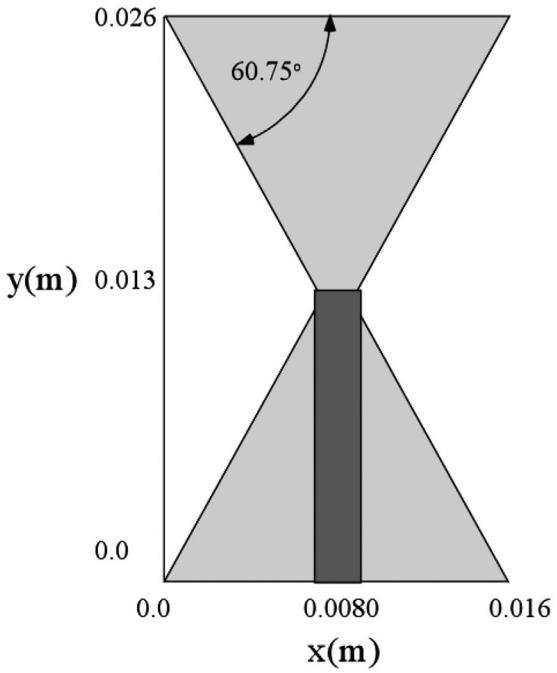

FIGURE 1 | Geometry used in Rocky.

corresponding to all particles having zero velocity), it would not start immediately discharging before an external force had been applied. The simulation was set up so that the stopper was removed at the same time as the vibrating force was applied.

As further shown in Figure 1, the hopper is of a symmetrical design, with the material discharging through the orifice of 2 mm diameter to the lower chamber.

The hopper wall angle was selected as 60.75° with respect to the horizontal axis, corresponding to a hopper half-angle (the angle measured between the inclined wall and the vertical centerline) of 29.25°. This value was not chosen arbitrarily but was determined in the attempt to promote a stable mass-flow regime while minimizing the likelihood of particle jamming and arch formation.

Along these lines, it is also worth recalling that the flow regime is a key factor governing the discharge behavior of granular materials [49]. In a mass-flow regime, all material within the hopper is mobilized during discharge, resulting in a relatively uniform and predictable flow rate [50]. Conversely, funnel flow may develop when only the material directly above the outlet is discharged while stagnant zones remain adjacent to the hopper walls, a phenomenon promoted by particle interlocking, particle-wall interactions, and geometric constrictions [51]. Since the objective of the present study was to investigate regolith discharge under controlled conditions, a configuration theoretically supporting the mass-flow regime has been targeted.

Previous studies have shown that hopper geometry strongly influences the transition between funnel flow and mass flow [52]. The transition depends on both the hopper wall angle and the particle-wall friction angle. Based on the measured mechanical properties of lunar regolith simulants, in particular, mass flow is expected when the hopper wall angle is sufficiently steep and the particle-wall friction angle remains below a critical value [53]. Accordingly, for the present hopper geometry, characterized by a half-angle of 29.25°, mass flow is expected provided that the wall friction angle is less than approximately 20° [53, 54]. Furthermore, the selected wall inclination is considerably steeper than the transition value of approximately 45° identified by Ahn et al. [52], thereby favouring mass-flow conditions throughout the discharge process.

Similarly, we select the outlet diameter according to established criteria for granular discharge. In such a context, it is worth recalling that the Beverloo's law [55] relates the mass discharge rate of granular materials to the outlet geometry according to $W = C\rho_B(g)(D_h - \phi d)^{5/2}$ where C is a material-dependent discharge coefficient, ρ_B is the bulk density, g is gravitational acceleration, D_h is the outlet diameter, d is the particle diameter, and ϕ is an empirical fitting parameter. This relationship is generally valid when the outlet diameter significantly exceeds the particle diameter [55]. For the lunar regolith simulant considered here, having a mean particle diameter of approximately 90 μm, the 2 mm outlet produces an orifice-to-particle diameter ratio of R ≈ 22. This ratio is substantially greater than the critical value reported by To et al. [56], who showed that the probability of jamming becomes negligible when the outlet diameter exceeds approximately five particle diameters. Consequently, arch formation and flow interruptions are not expected. The selected outlet diameter therefore satisfies the conditions required for continuous discharge and ensures that the principles governing the Beverloo's law remains applicable [57].

In light of these arguments, a 60.75° wall angle and a 2 mm outlet diameter were therefore selected to maximize the likelihood of stable mass flow, minimize stagnant regions and jamming events, and provide discharge conditions that can be reliably predicted using established granular-flow correlations. The initial mass of particles was chosen to be 52 mg of material, as this would occupy much of the upper chamber of the hopper

3 | Methods and Materials

3.1 | DEM

The discrete element method is used to determine the simulant material's behavior. This approach, DEM for short, was first developed by Cundall and Strack in 1979 as an extension of the Finite Element Method to model disk and spherical particles [58]. DEM is often used in engineering to model and predict the dynamics of bulk solids undergoing transformation or deformation, hence for a dispensing system such as a hopper, it can be regarded as an accurate modeling tool. The equations of motion for each particle are integrated numerically. This requires the resultant forces acting on the particle to be known. Resultant forces in this case consist of "body" forces and "contact" forces [59]. Body forces acting on a particle generally include the force of gravity. Contact forces include interaction between particles, and particle interaction with the boundary, that is, silo or hopper walls. In DEM, these contact forces are determined from the overlap between particles, or between particles and walls. Although particles are treated as discrete rigid bodies, a small virtual

overlap is allowed when contact occurs. This overlap represents the local deformation that would take place in real particles and is used to calculate the normal and tangential contact forces through an appropriate contact paradigm.

Some authors such as Castañeda et al. [60] have successfully used the Ansys Rocky DEM package for simulating lunar regolith. In Rocky, the equations of motion for particulate matter in DEM simulations are derived from Newton's Second Law (Equation 5) and Euler's equation (Equation 6) to describe the translational and rotational motion, respectively [61]. The general DEM solution cycle, as defined by Cundall and Strack [58] and Anandarajah [62] involves first calculating the overlap velocities between any particle pairs from the initial velocity [61], an explicit numerical scheme is then used to calculate the particle displacements during the time step. The contact models are applied to find the inter-particle forces [59], the equations of motion are then used to find the particle acceleration. Enough information is found to update the new location of each particle, and the cycle repeats. El-Emam et al. [61] provide a description of Newton's and Euler's equations of motion in a general form applied in DEM modeling as follows:

$$m_i \frac{d^2 \underline{r}_i}{d\tau^2} = \underline{F}_i^g + \sum_{j=1}^{N} \underline{F}_{ij}^c \tag{5}$$

$$I_i \frac{d\underline{\omega}_i}{d\tau} = \sum_{j=1}^{N} \underline{M}_{ij}^c \tag{6}$$

where m_i is the mass of particle i, and the vectors $\underline{r}_i$ and $\underline{\omega}_i$ denote its position and angular velocity, respectively. $\underline{F}_i^g$ is the body force acting on each particle due to gravity, $\underline{F}_{ij}^c$ and $\underline{M}_{ij}^c$ are the contact force and moment that particle j exerts on particle i, respectively; moreover, I_i is the moment of inertia of particle i (no interstitial fluid is simulated, hence no fluid-dynamic forces are considered). A simplifying assumption for the simulations here is that gravity is the only body force acting on the regolith particles. The gravitational force is simply given by:

$$\underline{F}_i^g = m_i \underline{g} \tag{7}$$

Vibrations are incorporated by imposing a time-periodic displacement on the physical boundary of the particle container. As outlined before, DEM computes the additional surface forces as the sum of elastic-plastic (normal) and frictional (tangential) components:

$$\underline{F}_{ij}^c = \underline{F}_{ij}^n + \underline{F}_{ij}^t \tag{8}$$

In the case of particle-particle or particle-boundary interactions, the normal and tangential directions are relative to the contact plane which intersects the contact location. In this study, the contact models were chosen based on relevant literature involving lunar regolith, used directly by Hasan and Alshibli [63] and Młynarczyk et al. [46], and employed similarly by refs [64–67]. In particular, the chosen normal surface contact force model is the Hysteretic Linear Spring model. This model, developed by Walton and Braun [68] was used in previous work involving JSC-1a by [63]:

$$\underline{F}_{ij}^{n,(\tau)} = \begin{cases} \min\left(\underline{F}_{ij}^{n,(\tau-\Delta\tau)} + K_u^n \underline{\Delta S}^n, K_l^n \underline{S}^{n,(\tau)}\right) if \Delta S^n \geq 0 \\ \max\left(\underline{F}_{ij}^{n,(\tau-\Delta\tau)} + K_u^n \underline{\Delta S}^n, K_l^n \underline{S}^{n,(\tau)} x10^{-3}\right) if \Delta S^n < 0 \end{cases} \tag{9a}$$

$$\underline{\Delta S}^n = \underline{S}^{n,(\tau)} - \underline{S}^{n,(\tau-\Delta\tau)} \tag{9b}$$

where $\underline{F}_{ij}^{n,(\tau)}$ and $\underline{F}_{ij}^{n,(\tau-\Delta\tau)}$ denote the normal contact force at times (τ) and (τ-$\Delta\tau$),, respectively, and $\underline{\Delta S}^n$ is the variation in overlap during the time frame $\Delta\tau$.

The loading and unloading stiffnesses [59, 63, 68, 69] are evaluated as:

$$\frac{1}{K_l^n} = \frac{1}{K_{li}^n} + \frac{1}{K_{lj}^n} \rightarrow K_l^n = \frac{K_{li}^n K_{lj}^n}{K_{li}^n + K_{lj}^n} \tag{10a}$$

$$\frac{1}{K_l^n} = \frac{1}{K_{li}^n} + \frac{1}{K_{lwall}^n} \rightarrow K_l^n = \frac{K_{li}^n K_{lwall}^n}{K_{li}^n + K_{lwall}^n} \tag{10b}$$

$$K_{li}^n = E_i d_i \tag{11a}$$

$$K_{lwall}^n = E_{wall} d_i \tag{11b}$$

where E_i is the Young's modulus, and d_i is the size of the contacting particles. The coefficient of restitution ε, related to energy dissipation, is given by:

$$\varepsilon^2 = \frac{K_l^n}{K_u^n} \tag{12}$$

We wish to highlight that, while this model does not explicitly resolve detailed contact-level phenomena such as local stress concentrations or micro-scale plasticity at corners, it remains suitable for the present study because the particles are represented as rigid polyhedral bodies. In this context, particle angularity and the associated corner interactions are explicitly resolved through the geometry of the bodies rather than through the constitutive complexity of the contact law. Consequently, the role of the contact model is primarily to provide a stable and physically consistent normal and tangential force-displacement relationship, rather than to reproduce detailed local deformation fields at contact points. DEM also models tangential forces induced by friction using a linear elastic-frictional model. The tangential force depends on whether sliding occurs [61]:

$$\underline{F}_{ij}^{t,(\tau)} = \min\left(\underline{F}_{ij}^{t,(\tau-\Delta\tau)} + K_l^n \underline{\Delta S}^t, \mu \underline{F}_{ij}^{n,(\tau)}\right) \tag{13}$$

where $\underline{F}_{ij}^{t,(\tau)}$ and $\underline{F}_{ij}^{t,(\tau-\Delta\tau)}$ are the tangential contact forces at times (τ) and (τ-$\Delta\tau$), $\underline{\Delta S}^t$ the tangential overlap change, and μ is the friction coefficient.

$$\mu = \begin{cases} \mu_s \; if \; no \; sliding \; (static \; coef f cient) \\ \mu_d \; if \; sliding \; (dynamic \; coef f cient) \end{cases} \tag{14}$$

Sliding occurs when the tangential force exceeds this threshold, reverting to non-sliding when below it.

All equations have been integrated numerically using an explicit scheme in time, allowing the complete history of particles in

the domain to be reconstructed (providing detailed information rarely accessible through experimental analysis). In this regard, we wish to highlight that because particles are treated in a distinct way and solved independently, and since they will only interact at contact points during overlap, hence the time step applied to the simulations must be small enough to allow for accurate contact force modeling [70]. Rocky [59] determines the DEM timestep by estimating the shortest contact event that can occur in the system. For each possible particle-particle and particle-wall interaction, it computes an equivalent mass-spring system based on the selected contact model (e.g., Hertz-Mindlin or linear spring-dashpot). The critical contact stiffness is obtained from the material properties and particle geometry, and the corresponding contact period is estimated. Rocky then selects the smallest contact period among all potential contacts and sets the timestep as a safe fraction of that value, ensuring that each collision is resolved with sufficient temporal resolution for numerical stability and accuracy. Thus, the timestep is automatically linked to the highest contact frequency in the granular assembly and scales approximately as $\Delta t \propto (m_{eff}/k_{eff})^{1/2}$, where m_{eff} is the effective mass of the contacting pair $[m_i m_j/(m_i+m_j)]$ and k_{eff} is the effective contact stiffness (evaluated through Equation (10)). The timestep is therefore related to the natural oscillation period of the stiffest and lightest contact that can occur in the system. Rocky examines all particle-particle and particle-wall combinations and selects the most restrictive case.

3.2 | Material Properties

Relevant numerical modeling requires the adoption of representative mechanical properties of lunar regolith and its simulants, as these parameters govern stress transmission, shear resistance, and overall flowability [71], and are therefore essential for predictive simulations [72, 73]. In particular, the handling and transport of regolith demand detailed knowledge of bulk mechanical behavior [13]. According to the literature, bulk densities of lunar regolith vary significantly with sampling location, ranging from approximately 0.74 to 1.75 g/cm^3 for Apollo 11 samples and from 1.35 to 2.15 g/cm^3 at the Apollo 15 site [74], indicating substantial spatial heterogeneity across mare and highland regions [75]. Experimental studies by [76] report uncompressed bulk densities between 1.4 and 1.8 g/cm^3 for both mare and highland samples, with a commonly cited mean lunar value of approximately 1.5 g/cm^3 [77].

The present work adopts the LHS-1 simulant, representative of lunar highland material [78]. Bulk density, often described as the degree of compactness, provides a practical estimate for bulk transport properties [79] and varies with packing history and compaction state [29]. The average LHS-1 bulk density provided by Exolith Lab [80] reads 1.34 g/cm^3.

However, density alone is not sufficient for characterizing the lunar regolith response. Its Young modulus, friction and restitution coefficients must also be specified.

About the Young's modulus of lunar regolith simulants, a range of values has been reported in the literature, reflecting strong sensitivity to testing conditions and material state. For JSC-1, values between 18 and 110 MPa have been indicated by Colwell et al. [81], while Alshibli and Hasan [71] observed a similarly broad range of 11.1-80 MPa. This variability is consistent with findings from Zou et al. [82] and Nie et al. [83], who show that stiffness is strongly dependent on confining pressure and bulk density. In particular, Zou et al. [82] report substantially lower effective moduli in the range of 99.39-593.65 kPa under low-confinement conditions, whereas indentation-based measurements by Nie et al. [83] yield significantly higher values, between 35 and 125 GPa, highlighting the strong influence of the measurement technique and stress state. In the context of the present hopper configuration, where particles are expected to experience varying degrees of confinement, with higher effective stress toward the lower regions and near the orifice and lower confinement near the free surface, an intermediate effective Young's modulus is assumed to be appropriate. Given the wide dispersion of reported values, a representative value of approximately 100 MPa is adopted, consistent with the upper range reported by Colwell et al. [81] and providing a reasonable compromise between the lower and higher estimates reported across the literature.

A more detailed discussion is needed to justify our selection for the friction coefficient and adhesive behavior. A precise evaluation of the shear properties of lunar regolith simulants can be found in the study by Yin et al. [84] where for dried LHS-1 they were reported (see Table 2 in their work) as a cohesion $c = 0.301 \pm 0.013$ (kPa) and an internal friction angle $\phi = 31.7° \pm 2.4$. This corresponds to a bulk friction coefficient of $\mu_{bulk} = \tan(31.7°) \cong 0.6$.

Using these data, the Mohr-Coulomb failure envelope of the material can be represented as $\tau = c + \sigma_n \tan(\phi) = 0.3 + 0.6\ \sigma_n$. In this formulation, the shear strength is composed of a constant cohesive contribution and a stress-dependent frictional contribution. The relative weight of these two mechanisms can be assessed by identifying the normal stress at which they become equivalent, obtained from $\sigma_n = c / \tan(\phi)$, which yields $\sigma_n \cong 0.48$ kPa. This value is extremely low in comparison with the stress levels typically encountered in granular assemblies, even under shallow deposits or weak confinement conditions. As a consequence, only in an exceedingly narrow low-stress regime does cohesion contribute comparably to the overall shear resistance. Once the normal stress exceeds this threshold, the frictional term rapidly becomes dominant, increasing linearly with confinement and quickly surpassing the constant cohesive offset. This scaling behavior indicates that the mechanical response of LHS-1 in the stress range relevant to most practical and numerical applications is governed almost entirely by inter-particle friction, while cohesion provides only a minor correction confined to near-zero confinement conditions. On this basis, and within the range of stress states relevant to the present simulations, we neglect cohesion as it does not materially alter the predicted shear strength or the macroscopic mechanical behavior of the material.

With regard to the friction coefficient itself, we assume for the DEM simulations a coefficients 0.35 for dynamic friction, 0.4 for the static friction. These values are clearly smaller than the aforementioned $\mu \cong 0.6$ but this choice stems from a precise rationale.

In DEM models of angular granular materials, the microscopic contact friction coefficient does not need to match the macro-

scopic friction coefficient because the bulk shear strength is an "emergent property" of the particle assembly rather than a direct expression of the Coulomb law at individual contacts. While the microscopic coefficient governs resistance to sliding at a single contact, the macroscopic response reflects additional mechanisms operating at the grain scale. In particular, for nonspherical particles, geometric interlocking between faces, edges, and vertices imposes strong kinematic constraints that inhibit relative motion even under moderate contact friction. This effect is reinforced by the development of anisotropic force chains, which organize stress transmission along preferential load-bearing paths and enhance stability under shear. Moreover, angular particles suppress rolling and rotation, increasing dissipative mechanisms beyond pure sliding friction, while macroscopic deformation requires coordinated rearrangements of many grains rather than isolated contact events. As a result, the experimentally measured bulk friction coefficient already incorporates contributions from both interparticle friction and particle morphology. When angular particle shapes are explicitly resolved in DEM, part of the macroscopic shear resistance is therefore provided by geometry rather than by the contact law alone, allowing the microscopic friction coefficient to be lower than the bulk value. The parameter choices adopted in this work follow this physical rationale, and are intended to reflect a consistent separation between contact-scale friction and shape-induced resistance. Nevertheless, these values are not intended as final calibrated parameters, and future work will refine them through systematic assessment against experimental measurements to further improve quantitative accuracy.

The particle model is defined using the mean diameter of the selected simulant material, approximately 90 μm. Nonspherical particles are employed instead of idealized spheres. These particles are represented here as polyhedral geometries. The adoption of nonspherical shapes improves physical realism, since angular particles generate multiple contact points, higher interlocking, and enhanced apparent cohesion. These effects significantly influence flow behavior, including an increased tendency for arch formation and orifice blockage (see, e.g., Garcimartin et al. [85] and Zuriguel et al. [86]).

For what concerns another characteristic parameter, that is, the restitution coefficient, existing evidence (see Chau et al. [87] and Table 1 in the much more recent study by Zhu et al. [88]) suggests that a value between 0.3 and 0.9 should be assumed. Although an intermediate value (e.g., ≅0.5) might be regarded as a reasonable choice, we intentionally adopt a value close to, and even slightly below, the lower bound of this range (0.2) in view of the considered particle size distribution (PSD). In real lunar regolith and in high-fidelity simulants, the granular assembly includes a substantial fraction of very fine particles, extending well below the micrometric scale (sub-micron fractions), which play a significant role in enhancing energy dissipation during collisions through increased surface interactions, asperity-level deformation, and frictional losses. In the present model, however, the adopted particle size distribution does not resolve these very fine constituents, thereby effectively filtering out a key physical source of dissipation associated with small-scale grains.

From a physical standpoint, the coefficient of restitution is not strictly a material constant, but exhibits an effective dependence on particle size because energy loss mechanisms vary with scale. As particle size decreases, the relative importance of surface effects, micro-asperity deformation, and contact-level dissipation increases, generally leading to lower restitution values. By contrast, the absence of the finest particles in the numerical representation reduces the overall dissipative capacity of the system and would otherwise lead to unrealistically elastic collisions and excessive kinetic energy retention. For this reason, reducing the restitution coefficient is introduced here as a compensatory modeling choice, aimed at restoring a realistic level of energy dissipation at the assembly scale and ensuring that the macroscopic dynamical behavior remains consistent with that of actual lunar regolith systems.

TABLE 1 | Discharge time, average mass flow rate and particle velocity at the amplitude peak for $\Gamma = 2$ as a function of the shaking frequency.

Frequency (Hz)	Discharge Time (seconds)	Mass Flow rate (g/s)	Velocity at Amplitude peak (m/s)
10	0.278	0.236	0.624
25	0.196	0.265	0.301
50	0.168	0.309	0.502
75	0.170	0.312	0.502
100	0.159	0.327	0.506
150	0.157	0.331	0.503
200	0.156	0.333	0.428
300	0.158	0.329	0.530

A final aspect requires discussion. Regarding particle shapes, Castañeda et al. [60], Garboczi [89] and Lane et al. [90] classified DEM particle morphologies for lunar regolith which are asymmetric and polyhedral, so similar particle geometries native to Rocky are used here and modified to create a simulant analogue (see also Mirghasemi et al. [91] and Govender, et al. [92]). A relevant model has to represent both larger and more "jagged" materials, but also the much finer particles which become more rounded from geophysical effects [93]. Along these lines, we have focused primarily on monodisperse particle mixtures, while secondary simulations have involved a polydisperse particle arrangement as further discussed in the results section. The considered distribution consists of a "standard size" mean diameter particle and differentiated particles to represent the size distribution of the simulant.

Past polydisperse DEM approaches to lunar regolith have involved 2 [94], 5 [95], and 6 [96] species simulations. Berger and Hrenya [95] and Bajpai et al. [96] used a much larger distribution of sizes, up to 1 mm and 10 mm respectively. Liever and West [94] used 30 μm and 100 μm particles. To compare both the monodisperse and polydisperse simulations, the mass discharge must be equal for both, hence the mass fractions for the polydisperse simulations must equal the total mass of the single particle simulations. The trade-off with including different-sized particle is that smaller particles of the same mass will have a

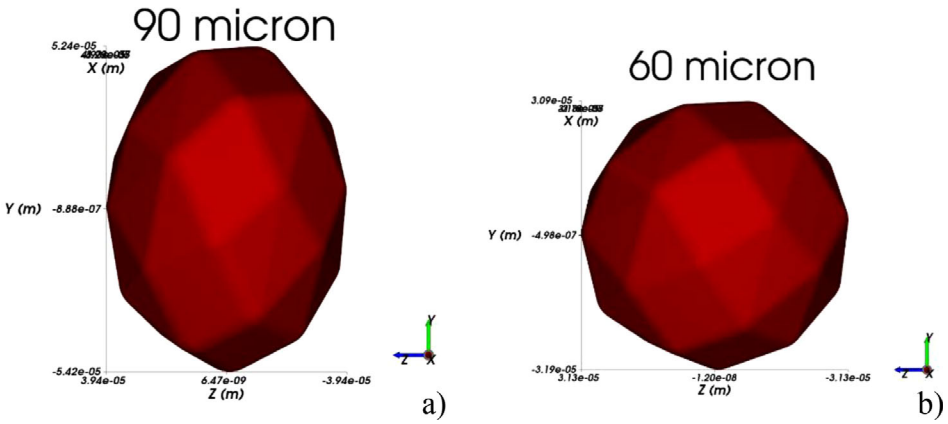

FIGURE 2 | Images of the two particles used in Rocky. a) the 90-micron polyhedron particle used in the monodisperse simulations (also used as the majority of the bulk particle mass in the polydisperse simulations), b) Sphero-polyhedron particle used for the polydisperse simulations only.

greater number of individual particles, increasing the simulation time, and including larger particles at the expense of the mean-sized particles can reduce the accuracy. To account for this, the mass fraction must generally include only a smaller proportion of the polydisperse mixture, replicating the "sieve-size" PSD of LHS-1 [80].

For the "average" LHS-1 particle, here, the sphero-polyhedron design shown in Figure 2a was chosen. The number of corners for the particle was increased from the default value of 25 to 30 corners because this would improve contact force detection when the particles overlap and increase the chance of particle interaction with more contact points. As explained before, the particle's mean diameter is 90 μm, as provided by Exolith Lab [80] and Long-Fox et al. [97]. The particle design is such that it has a vertical aspect ratio of 1.10 (0.9 according to the notation by [98]), and a horizontal aspect ratio of 0.75. These values are in line with the outcomes of the image analysis performed by Rickman et al. [98] who showed that the aspect ratio ranges between 0.61-0.9. Similarly, Zhou et al. [47] considered a range 0.5-0.95 in their simulations. The slightly asymmetric design covers both larger agglomerates which are highly asymmetric, and smaller dust particles which may be nearly spherical in nature. A second simulant particle was created to test a bi-disperse simulation (Figure 2b). This particle, with size 60 μm, was also chosen to be a sphero-polyhedron, with their number accounting for 10% of the total mass, hence, resulting in a particle count that represents over a quarter of the total number of particles. To model the weathering which smaller particles experience, however, the horizontal and vertical aspect ratios were set to 1.0, making it more symmetrical than the standard 90 μm particle. In this regard, it is worth recalling that, in general, smaller lunar regolith particles tend to be more rounded than larger ones, although the trend is not perfectly monotonic and depends on lithology and exposure history. This tendency is consistently reported in analyses of Apollo lunar soil samples and is linked to the dominant space weathering processes and fragmentation mechanics that control regolith evolution. Larger lunar particles are angular because they form mainly through brittle fragmentation from micrometeorite impacts. With decreasing size, repeated comminution, impact gardening, and thermal fatigue progressively smooth grains. Space weathering and agglutinate formation further round fine particles, producing a more equant morphology in the smallest regolith fractions (see, e.g., Pieters and Noble [99]).

As explained in Sect. 2.2, the initial mass of particles was chosen to be 52 mg of material, as this would occupy much of the upper chamber of the hopper. Accordingly, the number of particles was 61000 for the monodisperse case and 74929 particles for the bi-disperse case, respectively.

The simulated physical time was 0.5 s for each case, a duration selected to ensure sufficient time for particle settling within the hopper. The hopper plug remained in place for the first 0.1 s, which was found to be adequate for the particle bed to stabilize in the upper section of the hopper. After this period, the plug was deactivated, equivalent to its removal in a corresponding physical experiment. As discussed further in Sect. 4, the remaining 0.4 s was sufficient for nearly all cases to discharge the residual particles, and therefore the simulations were not extended beyond this duration. All simulations were performed using an effective time step of approximately $\cong 2\times10^{-8}$ s, resulting in a computational time of approximately 48 h per simulation on an NVIDIA A100 GPU.

4 | Results

This section is entirely used to present the numerical results obtained with the method and underpinning models described in Sects. 3 and 2, respectively. In particular, these are articulated in three different groups for increasing values of the non-dimensional parameter Γ (namely, Γ = 2, 4 and 6). Each case is characterized quantitatively through the metrics defined in Sect. 2.1 and qualitatively in terms of patterning behavior. Cross comparison between monodisperse and bi-disperse cases is also implemented as necessary before some general trends are finally distilled out in Sect. 5.

4.1 | Moderate Gamma (Γ = 2)

4.1.1 | Monodisperse Case

The results for Γ = 2 are collected in Table 1, which summarizes relevant data such as the required discharge time, average mass

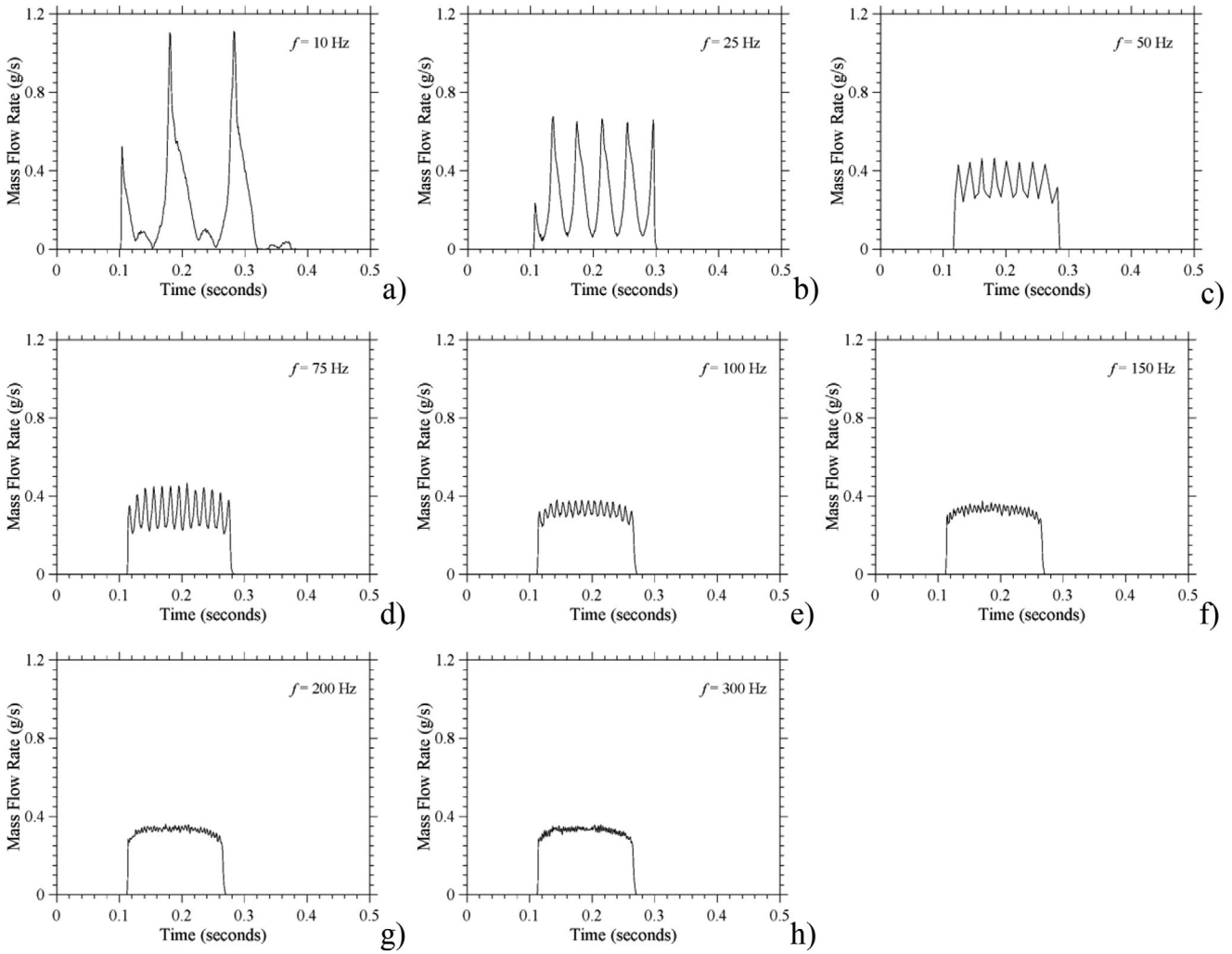

FIGURE 3 | Instantaneous Mass flow rate vs time for $\Gamma = 2$ and different frequencies: (a) 10 Hz, (b) 25 Hz, (c) 50 Hz, (d) 75 Hz, (e) 100 Hz, (f) 150 Hz, (g) 200 Hz, (h) 300 Hz.

flow rate and velocity at the amplitude peak, and Figure 3 where the instantaneous mass flow rate is plotted as a function of time for the frequency of the imposed vibrations spanning the range 10 Hz $\leq f \leq$ 300 Hz.

What stands immediately out from this figure is that, in general, the instantaneous mass flow rate oscillates in time with the same frequency of the imposed vibrations. However, as the frequency f increases and amplitude b decreases accordingly (to keep Γ constant), the amplitude of the instantaneous mass flow rate also decreases.

In particular, at 10 Hz, the particles reach a maximum flow rate of 1.1 g/s, with 3 major peaks visible in the discharge cycle and 2 smaller local minima. The 25 Hz simulation shows that the peak mass flow rate has been reduced to approximately 0.68 g/s (Figure 3b), a noticeable decrease from 10 Hz. The number of discharging peaks is larger (as expected), and the time taken to dispense the material becomes smaller. The average mass flow rate rises accordingly from 0.236 g/s to 0.265 g/s. This trend continues at 50 Hz, where the value of the mass flow rate is 0.309 g/s. Most interestingly, as made evident by the dimensionless discharge shown in Figure 4, at 50 Hz the flow

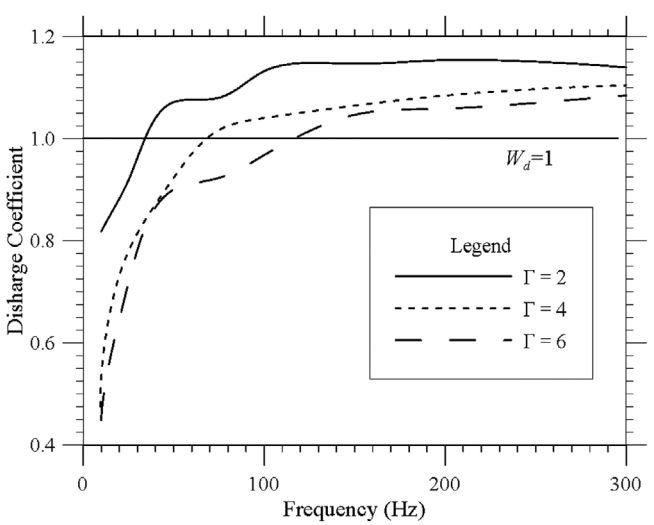

FIGURE 4 | Dimensionless discharge rates W_d as a function of vibrational frequency for different values of Γ. A discharge coefficient greater than 1 indicates a flow regime which can discharge at a rate larger than that of a purely gravity driven flow.

rate displays an improvement with respect to a gravity-driven discharge (no imposed vibrations). There is not much change at 75 Hz, but a growth can be noticed again by 100 Hz. Between 100 Hz and 300 Hz, the mass flow remains consistent, ranging between 0.327 g/s at 100 Hz and 0.333 g/s at 200 Hz. The most notable increase occurs between 50–100 Hz.

It is also worth highlighting that the time taken to discharge the material completely is consistent across all frequency ranges, decreasing only slightly from 50–300 Hz. The mass flow rate from gravity alone was found to be 0.289 g/s. Overall, as implicit in the arguments provided above, the dimensionless discharge rate (Figure 4) indicates that over most of the considered frequency range at $\Gamma = 2$, the flow rate consistently improves with respect to the purely gravitational one.

With regard to patterning behavior, the flow properties of the simulated regolith, sampled at selected frequencies, can be seen in Figure 5. The distribution of particle velocity revealed by the panels of this figure, was obtained by tracking the absolute translational velocity of the particles (in particular, we show the velocity fields at the maximum and minimum amplitudes of the particle discharge cycle).

At 10 Hz, high levels of shearing can be recognized (Figure 5a). Funnel flow is noticeable in this case. In particular, at the minimum of the discharge cycle (Figure 5b) the regolith mass has separated from the hopper walls. In the central region just above the orifice, the particles are reaching a higher velocity (light blue) than those immediately surrounding the walls (dark blue).

At 50 Hz the velocity field shows the regolith discharging mainly from the center of the hopper, forming an appearance most akin to funnel flow (Figure 5c,d). The higher velocity particles (light blue) are located in the center of the continuum of particles for both frames. In particular, Figure 5c shows the particles closest to the hopper wall have a lower velocity. As this is the amplitude peak of a vibration cycle, the particles closest to the hopper wall have rebounded, their inertia relative to the hopper movement resulting in a lower apparent velocity. Figure 5d shows the amplitude trough. In this case, the entire regolith continuum is at a higher velocity as it travels downwards, including at the center and top of the flow field. This is also characteristic of funnel flow. Also notable is the separation of the particles from the hopper wall.

Overall, these figures demonstrate that the maximum and minimum velocities within the hopper vary during the oscillation cycle. At 50 Hz, the maximum and minimum velocities were 21.4 cm/s and 2.7 cm/s at the amplitude trough. Whilst at the peak amplitude, the maximum velocity reached 22.7 cm/s, and the minimum was 0.04 cm/s, indicating a highly stagnant flow condition.

At 100 Hz, (as shown in Figures 5e,f) the velocity fields become highly similar at the maximum and minimum amplitude. The amplitude trough shows a higher velocity of particles at the top of the mass of regolith, and a localized ratholing behavior is visible at the center (manifesting as a divot, that is, a cusp-like point highlighting the presence of a small localized depression on the top surface of the granular material). For these conditions, at the peak of the vibration cycle, the particles reached a maximum velocity of 23.1 cm/s and a minimum of 0.2 cm/s. Maximum and minimum velocities of 22.5 and 0.17 cm/s were reached at the amplitude trough.

TABLE 2 | Mass Flow Rate Comparison.

f (Hz)	W [monodisperse] (g/s)	W [bi-disperse] (g/s)
25	0.265	0.266
50	0.309	0.302
100	0.327	0.311

Finally, the 300 Hz simulation (Figures 5g,h) indicates that the maximum and minimum of the vibration cycle are almost indistinguishable from one another and bear a similar resemblance to the 100 Hz simulation. For the duration of the simulation at 300 Hz, the particles at the top of the mass are constantly funneling down the center and out of the orifice, with particles closer to the hopper wall moving at a lower velocity. The maximum velocity reached by the particles at peak amplitude was 22.8 cm/s; the minimum velocity reached in the hopper was 0.1 cm/s at the funnel walls; again, presenting nearly stagnant conditions.

4.1.2 | Bi-disperse Case

Bi-disperse particle mixtures were simulated at 25, 50 and 100 Hz. The corresponding results, analogous to those shown in Figure 3 for the monodisperse case, do not exhibit significant differences compared with the monodisperse simulations; for this reason, they are not reported here. In particular, at 50 Hz, we observed a marginal increase in the average flow rate compared with the monodisperse case (the related values being 0.309 and 0.302 g/s for mono- and bi-disperse cases, respectively). At 100 Hz the trend was also very similar to the monodisperse case, discharging in the same amount of time.

Table 2 shows more precisely the comparison between the monodisperse and bi-disperse cases: At 25 Hz, the two different particle mixtures display almost identical values of W, namely, 0.266 g/s and 0.265 g/s. This increases to the aforementioned values at 50 Hz and widens still at 100 Hz. The increase in mass flow values between each frequency is approximately the same for monodisperse and bi-disperse mixtures.

The corresponding particle patterns and related velocity fields are illustrated in Figure 6.

The 25 Hz (Figures 6a,b) simulation displays typical funnel flow characteristics. At the point of the maximum discharge, there is significant particle separation from the hopper wall, which is a common trend for high-amplitude simulations. The minimum of the discharge cycle indicates a high particle velocity (light blue) nearest the wall as the hopper moves up and compacts the particles. There is an area of slower-moving particles (dark blue) towards the center, while the particles nearest the orifice are travelling at a higher velocity again (light blue). In particular,

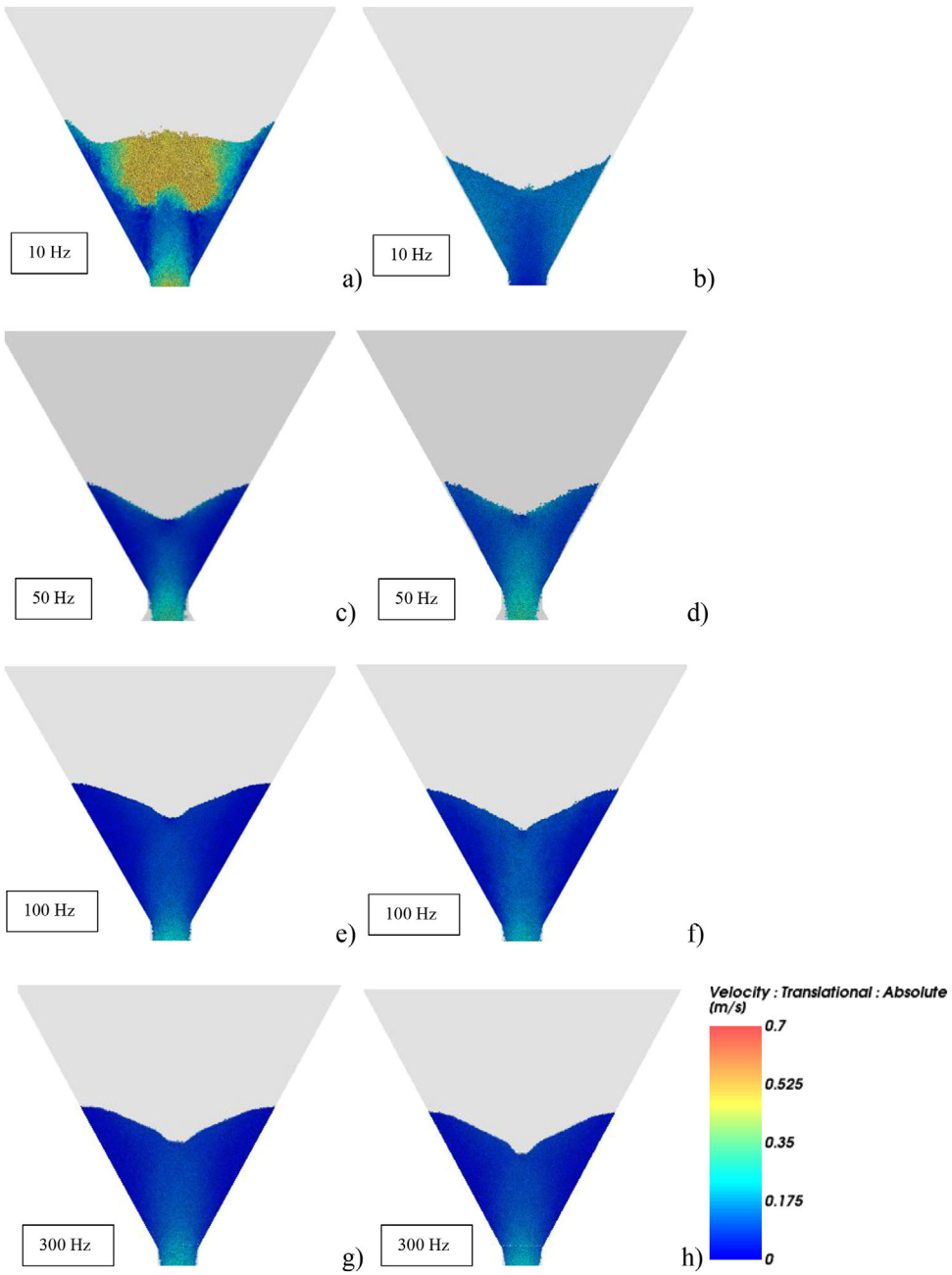

FIGURE 5 | Particle velocity contour maps for $\Gamma = 2$ (monodisperse case) and selected frequencies. (a) 10 Hz maximum discharge; (b) 10 Hz minimum discharge; (c) 50 Hz maximum discharge; (d) 50 Hz minimum discharge; (e) 100 Hz maximum discharge; (f) 100 Hz minimum discharge; (g) 300 Hz maximum discharge; (h) 300 Hz minimum discharge.

in Figure 6a it can be observed that the particles closest to the wall are the slowest-moving. Here the areas of dark blue towards the wall correspond to approximately 0.04 cm/s. The 50 Hz simulation (Figures 6c,d) has a flow behavior equivalent to that of the monodisperse particle mixture. The funnel flow and higher velocity dispersion in the center of the mass are still visible, as well as the small cusp point at the center of the continuum. The case 100 Hz (Figures 6e,f) is visually nearly identical to the monodisperse case as well. The higher velocity particles are present in the central mass above the orifice. A difference may be noted in the cusp point opening not being present at the top of the particle continuum.

4.2 | Intermediate Gamma ($\Gamma = 4$)

4.2.1 | Monodisperse Case

The simulation results for intermediate values of Γ ($\Gamma = 4$, see Figure 7 and Table 3) are consistent with the trends for $\Gamma = 2$. Nevertheless, an evident secondary frequency is visible at 10 Hz (Figure 7a) and 25 Hz (Figure 7b). Hereafter, we will refer to this extra response as the *intrinsic excitation frequency*.

Interestingly, however, at 50 Hz (Figure 7c), this extra frequency is no longer visible.

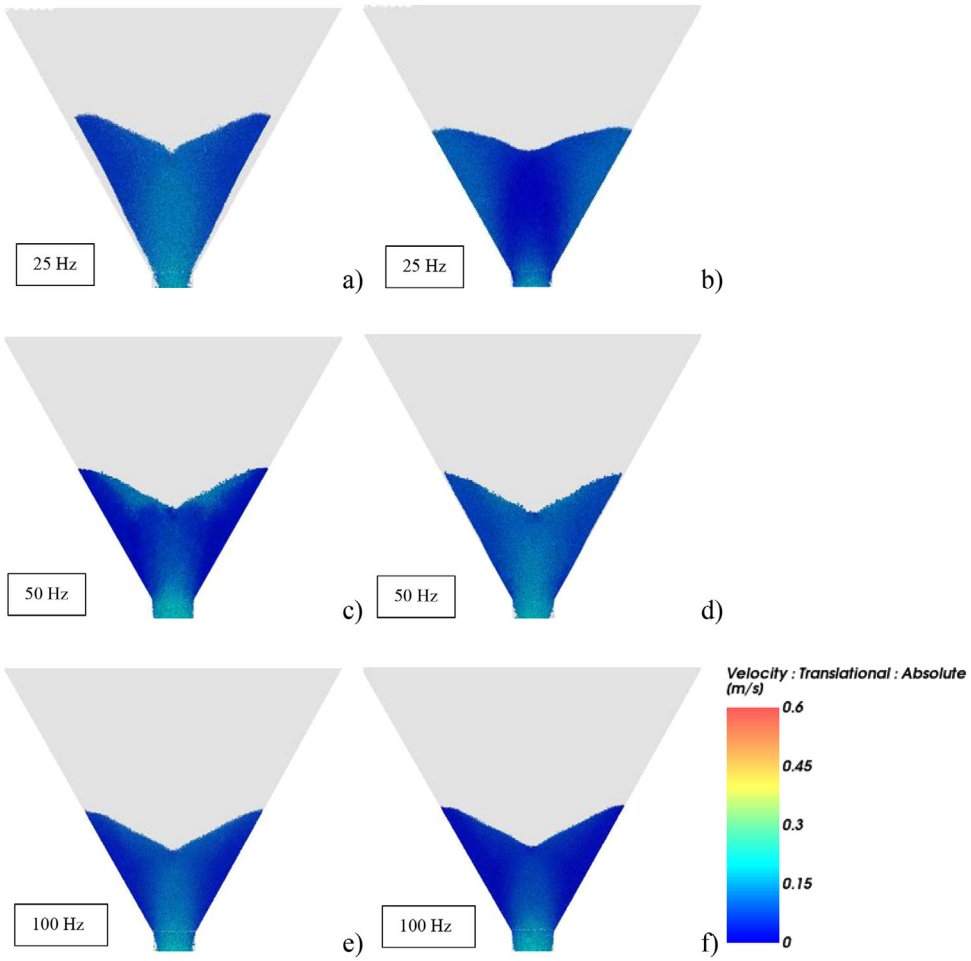

FIGURE 6 | Particle velocity contour maps for $\Gamma = 2$ (bi-disperse cases) and selected frequencies: (a) 25 Hz maximum discharge; (b) 25 Hz minimum discharge; (c) 50 Hz maximum discharge; (d) 50 Hz minimum discharge; (e) 100 Hz maximum discharge; (f) 100 Hz minimum discharge.

TABLE 3 | Discharge time, average mass flow rate and particle velocity at the amplitude peak for $\Gamma = 4$ as a function of the shaking frequency.

Frequency (Hz)	Discharge Time (seconds)	Mass Flow rate (g/s)	Velocity at Amplitude peak (m/s)
10	0.401	0.130	1.063
25	0.231	0.225	0.835
50	0.195	0.267	0.798
75	0.177	0.294	0.657
100	0.173	0.301	0.547
150	0.168	0.310	0.518
200	0.166	0.313	0.510
300	0.163	0.319	0.509

Another distinguishing mark of the 10 Hz simulation is the largest average particle flow, and simultaneously the lowest mass flow rate (the mass flow rate at 10 Hz is 0.129 g/s, reaching a maximum of 0.319 g/s at 300 Hz).

Notably, while the average mass flow rate at $\Gamma = 2$ was 0.326 g/s, at $\Gamma = 4$ this has decreased to 0.298 g/s. Superimposed on these observations is the realization that, as evident in Figure 8, at $\Gamma = 4$, the frequency range does not produce an improvement on a gravitational discharge until approximately 75 Hz (the reader being also referred again to Figure 4 for comparison).

These observations are complemented by the corresponding flow patterns in Figure 9. These are instrumental in revealing that the patterning behavior at $\Gamma = 4$ follows a trend as seen at $\Gamma = 2$. The funnel flow mode is present for all frequencies. In particular, at 10 Hz, the particle dynamics are highly fluidized and non-linear. The contour maps are shown in correspondence of the local maxima and minima visible in Figure 7a for both frequencies present, due to the aforementioned intrinsic excitation frequency (the interested reader being referred to Sect. 4.4 for a detailed analysis of the flow spectral content). Figure 9a relates to the first local maximum, with the regolith rising sharply from the central portion of the particle bulk. The material closer to the orifice (turquoise) is slower-moving at 0.69 cm/s, while the majority of the particles are travelling at 65.18 cm/s away from the hopper walls. In Figure 9c the regolith has formed a funnel flow pattern with a cusp point in the center of the particle mass. Higher velocity areas on the top of the continuum shown in light blue indicate particles "avalanching" towards the orifice.

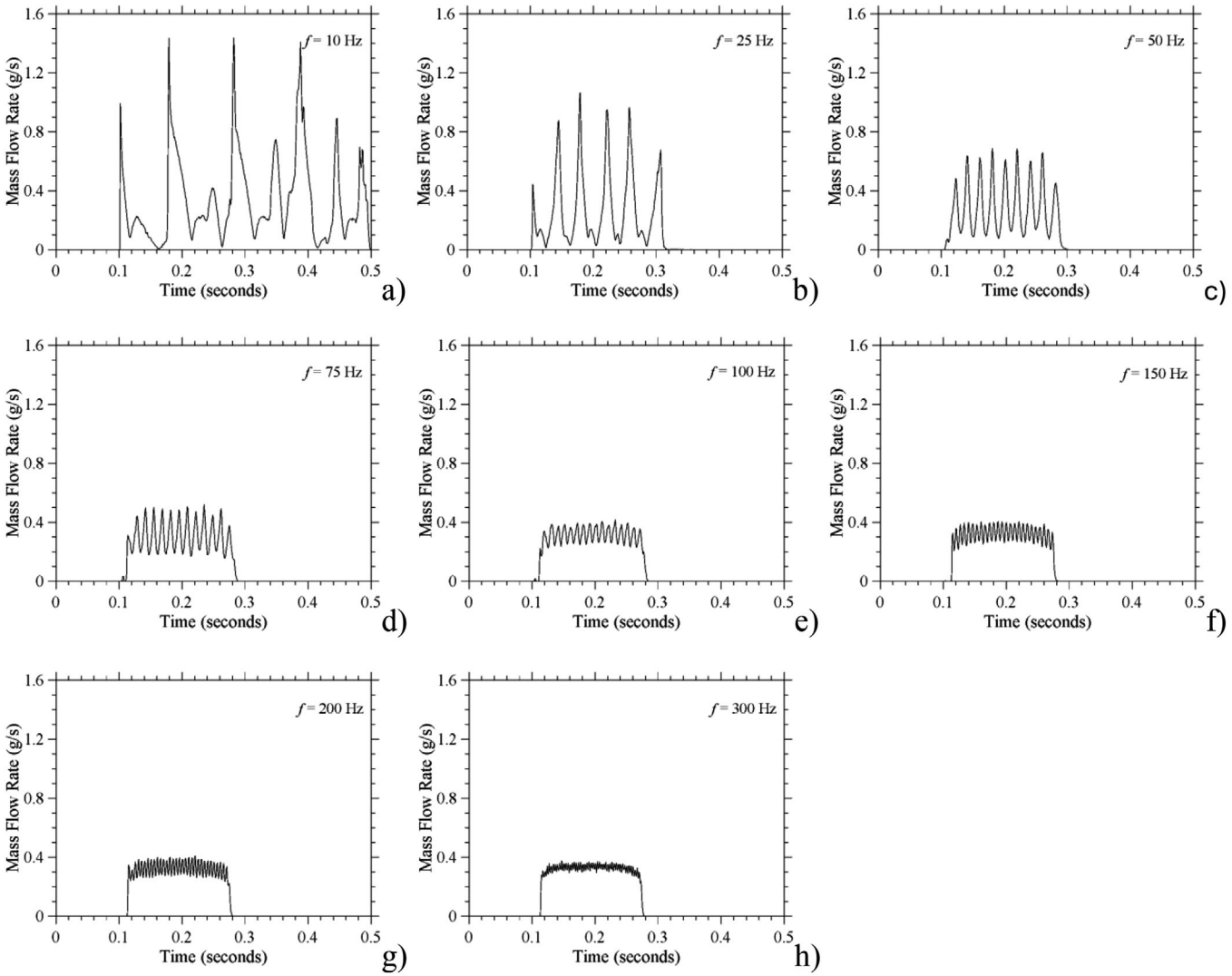

FIGURE 7 | Instantaneous Mass flow rate vs time for Γ = 4 and different frequencies: (a) 10 Hz, (b) 25 Hz, (c) 50 Hz, (d) 75 Hz, (e) 100 Hz, (f) 150 Hz, (g) 200 Hz; (h) 300 Hz.

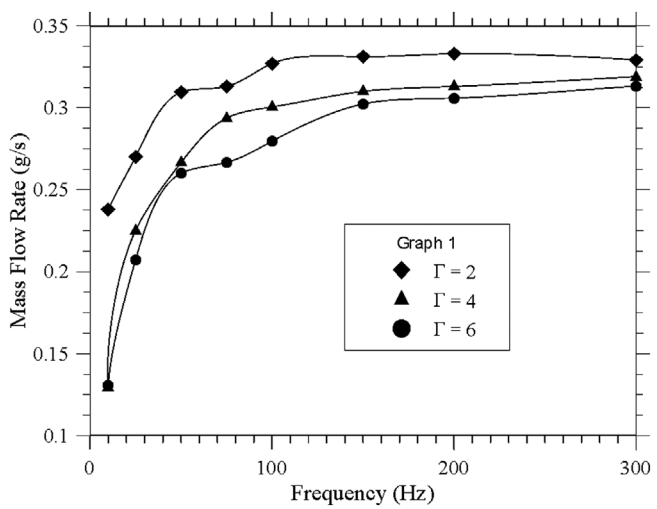

FIGURE 8 | Instantaneous mass flow rate for each discrete frequency interval for various values of Γ.

The material closest to the wall remains slow-moving (0.56 cm/s) whilst particles passing the orifice reach 101.95 cm/s, discharging a large portion of the mass very quickly. Figures 9c–d show the maxima and minima related to the secondary frequency. At the maximum, the particle dynamics are very similar to the primary maximum situation, but with a lower maximum particle velocity of 88.45 cm/s. The final frame at 10 Hz (Figure 9d) displays a highly chaotic, fluidized particle behavior. Here, the material is again sticking to the hopper walls, but with an arch formation between the two sides of the hopper. There is also material re-entering the orifice towards the arch. The particle velocities remain consistent with the first frame, reaching a maximum of 100.62 cm/s, and a minimum of 0.72 cm/s.

At 50 Hz (Figure 9e,f) the response of regolith is relatively similar to that seen in the Γ = 2 for the same frequency. The funnel flow mode is still evident together with a noticeable increase in the particle height from the hopper. The particle velocities at 50 Hz are consistent with each other, reaching 24.2 cm/s at the maximum, and 21.1 cm/s at the minimum. In particular, the slow-

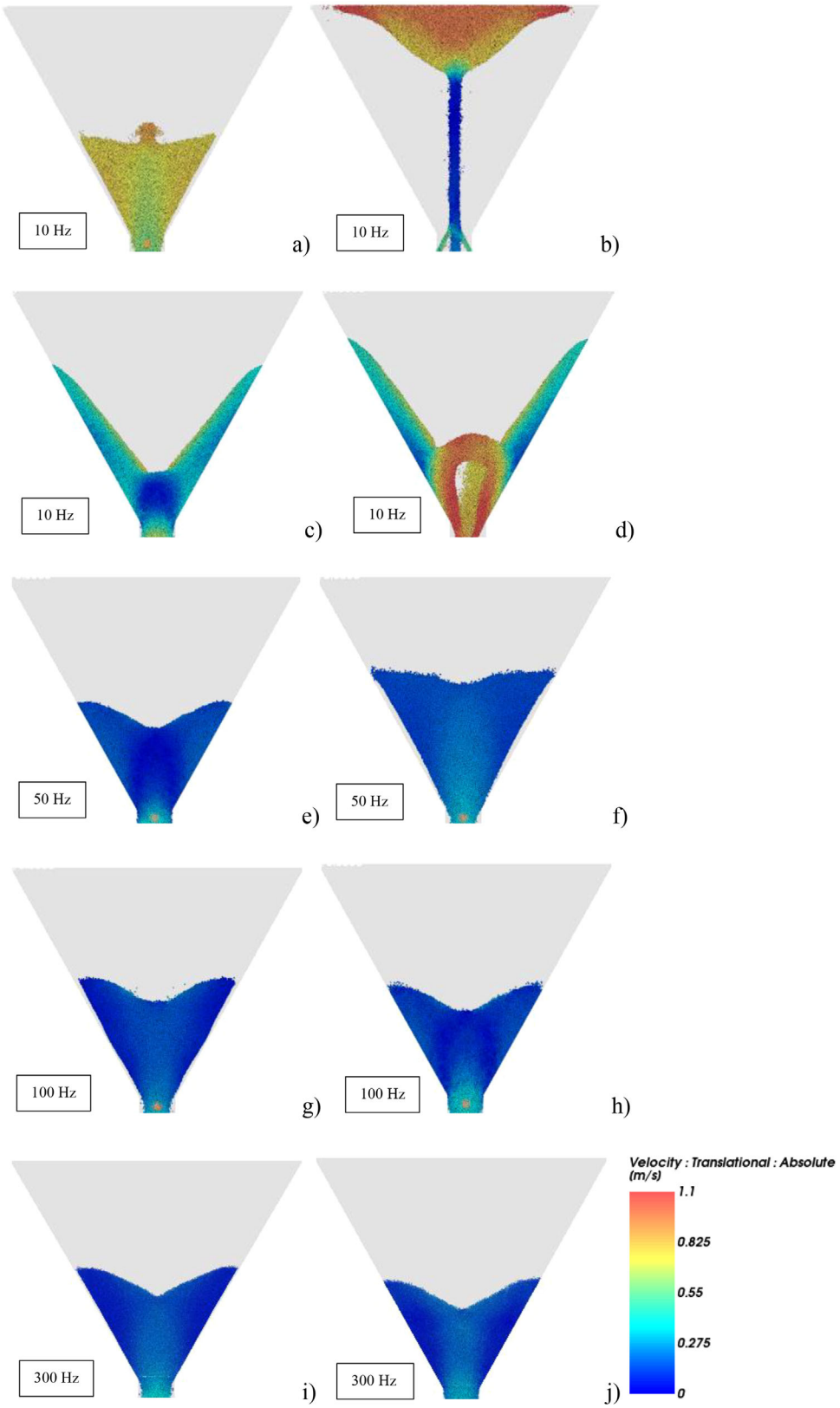

FIGURE 9 | Particle velocity contour maps for $\Gamma = 4$ (monodisperse case) and selected frequencies: (a) 10 Hz maximum velocity, main frequency; (b) 10 Hz minimum velocity, main frequency; (c) 10 Hz maximum velocity, secondary frequency; (d) 10 Hz minimum velocity, secondary frequency; (e) 50 Hz maximum discharge; (f) 50 Hz minimum discharge; (g) 100 Hz maximum discharge; (h) 100 Hz minimum discharge; (i) 300 Hz maximum discharge; (j) 300 Hz minimum discharge.

TABLE 4 | Mass flow rate comparison $\Gamma = 4$.

f (Hz)	W [monodisperse] (g/s)	W [bi-disperse] (g/s)
25	0.225	0.216
50	0.267	0.270
100	0.302	0.306

moving particle velocities are 0.07 and 0.04 cm/s at the peak and trough, respectively.

At 100 Hz the peak amplitude shows the particle velocities mostly constant across the continuum (Figure 9g), reaching a velocity as high as 22.1 cm/s. There is a stagnant area shown in dark blue, and central to that a light blue column indicating the central mass is discharging and the surrounding particles are slower moving. At the signal amplitude trough (Figure 9h) there is a subtle separation of particles from the bed, at a height close to that of the 50 Hz simulation at $\Gamma = 2$. At this minimum, much more of the particle mass is reaching a higher velocity in the center, whilst particles at the hopper wall remain slow-moving. Here the maximum velocity has increased to 23.3 cm/s.

Both frames (Figure 9i,j) of the 300 Hz simulation are in keeping with the $\Gamma = 2$ case. Here there is a dispersed mass of particles in the center, again displaying funnel flow, with slow-moving particles towards the hopper wall. There is little variation between the frames corresponding to peak and minimum of the signal shown in Figure 7h. For this frequency, the maximum particle velocity is equivalent for the peak and the trough at 23.1 cm/s, whilst the minimum velocities are 0.1 cm/s at the peak and 0.9 cm/s at the trough.

4.2.2 | Bi-disperse Case

As shown in Table 4, the bi-disperse particle flow rates display the major trends of the monodisperse simulations also followed, with quantitative differences being minimal.

The corresponding patterns are presented in Figure 10. Observing the 25 Hz simulations, there are high-velocity particles close to the wall in Figure 10a. The next frame then displays the high separation between the particles and the hopper (Figure 10b). At the peak of the secondary frequency, the particle velocity has slowed, and it is possible to recognize behavior indicative of funnel flow (Figure 10c). The final frame shows the secondary minima point (Figure 10d). The particles have reached a higher velocity (57.1 cm/s) and there is some shearing visible in the mass of particles, especially towards the top of the continuum where particles have separated from the mass.

Similarly, the 50 Hz and 100 Hz simulations (Figures 10e–h) mirror those of the monodisperse particles. The main difference is that since the number of particles has increased, the small cusp-like geometrical feature that begins at the center of the continuum of particles is absent. The funnel flow appearance is present in the bi-disperse case at these frequencies.

TABLE 5 | Discharge time, average mass flow rate and particle velocity at the amplitude peak for $\Gamma = 6$ as a function of the shaking frequency.

Frequency (Hz)	Discharge Time (seconds)	Mass Flow rate (g/s)	Velocity at Amplitude peak (m/s)
10	0.398	0.131	1.261
25	0.251	0.207	1.06
50	0.2	0.260	0.847
75	0.195	0.267	0.737
100	0.186	0.280	0.518
150	0.172	0.302	0.506
200	0.17	0.306	0.428
300	0.166	0.313	0.129

4.3 | High Gamma ($\Gamma = 6$)

4.3.1 | Monodisperse Case

As usual, all the plots for different values of the frequency have been collected in a single figure for $\Gamma = 6$ (Figure 11, see also Table 5). The instantaneous mass flow rate confirms that the average amplitude has increased with respect to $\Gamma = 4$ (Figure 7). Interestingly, however, this relation is true only up to 150 Hz. At 200 and 300 Hz, the amplitude visible in the plots remains lower than at $\Gamma = 4$ and attains values closer to those seen for $\Gamma = 2$. As expected, it becomes noticeably smaller as the frequency increases.

However, another important characteristic stands out from this figure. It can be seen that the discharge rate becomes more unpredictable. This is most noticeable at 200 and 300 Hz.

An additional noteworthy feature can be observed in the 10 Hz simulation (Figure 11a), where the material does not completely discharge within the simulated time interval, whereas complete discharge is achieved in all subsequent cases. This behavior can be attributed to the relatively large vibration amplitude associated with the 10 Hz condition. At this frequency, the particles attain a maximum velocity of approximately 1.8 g/s, the highest value among all simulations, resulting in pronounced particle rebounds from the internal hopper walls.

Furthermore, after passing through the orifice, particles remain in its proximity. The large oscillation amplitude therefore promotes particle recirculation, allowing some particles to be propelled back through the outlet and re-enter the upper hopper section. This reverse transport mechanism effectively reduces the net discharge rate and prevents complete emptying of the hopper during the simulated period.

Additional key observations concern the low-frequency simulation results. The aforementioned "intrinsic" excitation frequency is still present (Figures 11a and b).

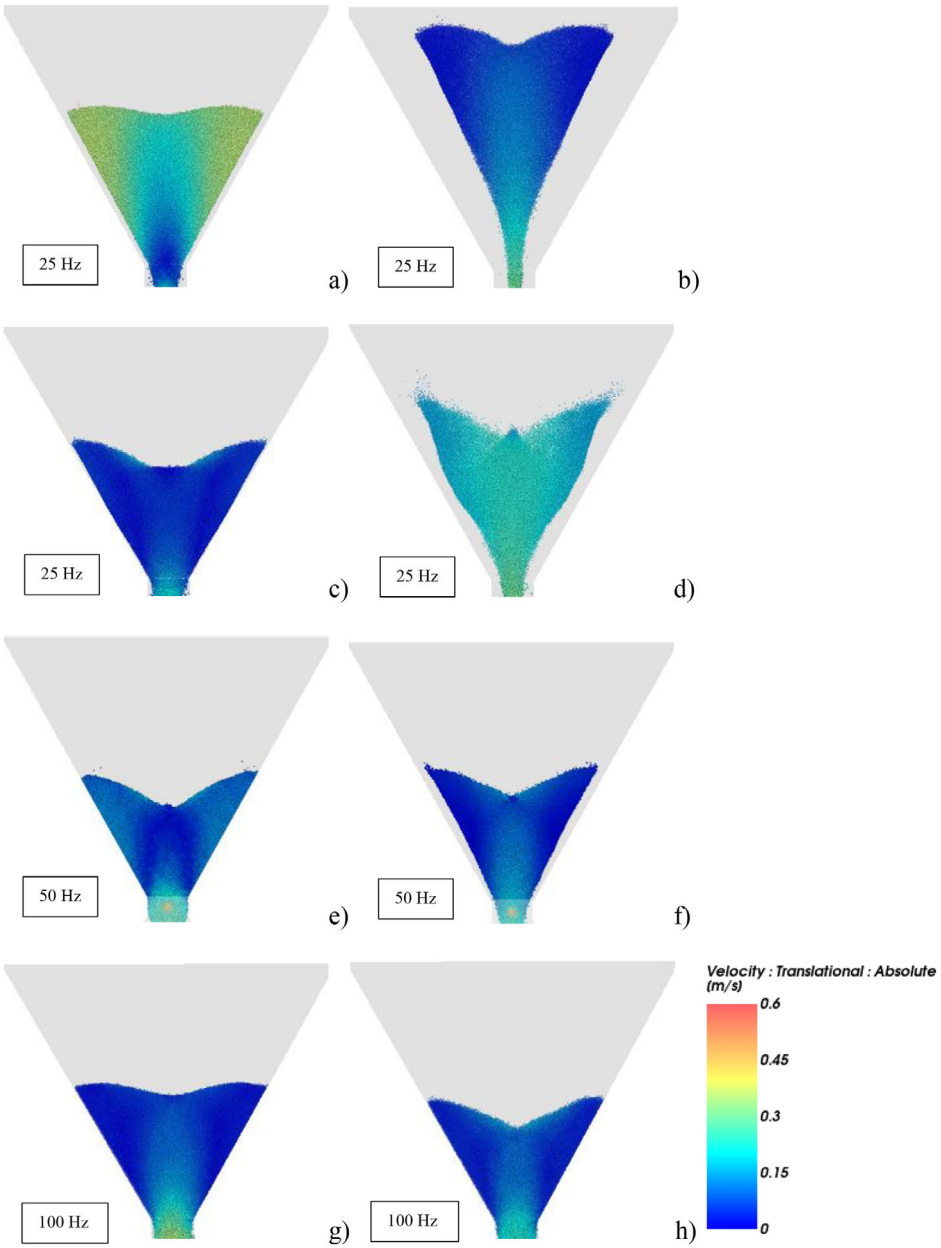

FIGURE 10 | Particle velocity contour maps for Γ = 4 (polydisperse case) and selected frequencies: (a) 25 Hz maximum discharge, main frequency; (b) 25 Hz minimum discharge, main frequency; (c) 25 Hz maximum discharge, secondary frequency; (d) 25 Hz minimum discharge, secondary frequency; (e) 50 Hz maximum discharge; (f) 50 Hz minimum discharge; (g) 100 Hz maximum discharge; (h) 100 Hz minimum discharge.

The mass flow rates across the entire frequency distribution can be seen once again in Figure 8. The mass flow rate increases between 10 and 50 Hz, then reaches a first plateau at 75 Hz. From this point, it continues to rise steadily up to 150 Hz, but at a much lower rate, before becoming constant again, forming a second plateau. Together with the previously shown Figure 4, where the dimensionless discharge W_d was plotted for each value of Γ, Figure 8 supports the realization that there are frequencies and values of Γ which are beneficial for a discharging hopper. Frequencies at Γ = 2 consistently produce W_d>1 for a frequency larger than 35 Hz, which indicates a positive discharge rate. For Γ = 4, W_d>1 after 75 Hz but does not reach values as high as those obtained for Γ = 2. For Γ = 6, the discharge rate does not improve on the purely gravitational case until ≈125 Hz and remains at a low level.

The corresponding dynamics in terms of patterning behavior also deserve attention and are presented in Figure 12, which includes more frames with respect to the earlier corresponding figures for smaller values of Γ because of the aforementioned intrinsic excitation frequency clearly recognizable in Figure 11. The apparent cohesiveness follows the same trend seen for Γ = 4. In Figure 12a (f = 10 Hz), the particles leave the bed as a continuum at a high velocity (88.2 cm/s). At the first local minima (Figure 12b), the avalanching response is observed again. Here the velocity of the particles exiting the orifice reaches a maximum of 126.5 cm/s. The slow-moving areas of particles remain at 0.78 cm/s, creating the largest discrepancy between maximum and minimum velocities of the simulations. The secondary-frequency discharge peak (Figure 12c) displays the material amalgamating at the top of the hopper, with a visible low-velocity stream re-entering

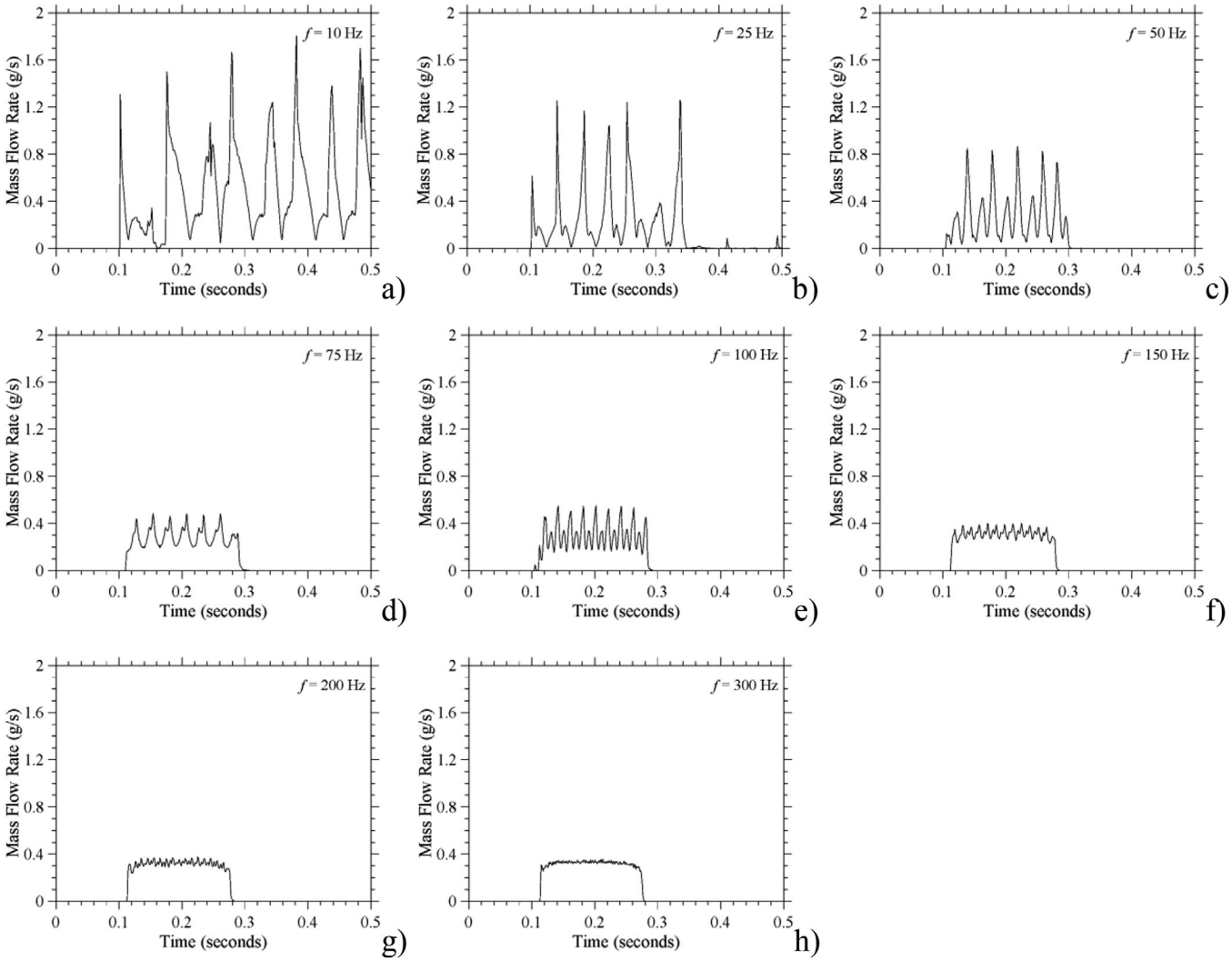

FIGURE 11 | Instantaneous Mass flow rate vs time for Γ = 6 and different frequencies: a) 10 Hz, b) 25 Hz, c) 50 Hz, d) 75 Hz, e) 100 Hz, f) 150, g) 200 Hz, h) 300 Hz.

the orifice. A highly fluidized state is attained at the lowest point of the vibration cycle, showing an arch's pre-formation (Figure 12d). At this stage, the velocity remains relatively high at 48.3 cm/s.

A fluidized state is still visible for the top layer of the particle mass at 50 Hz. For this value of Γ, the separation between the particles and the hopper is much more evident than for Γ = 2 and Γ = 4. Funnel flow is apparent at 50 Hz (Figures 12e–f & h), while mixing of particles of different velocities can be seen in Figure 12g. At 100 Hz (Figures 12i–l), the overall behavior mimics that of previous simulations at the same frequency. Funnel flow is observed with stagnant particles at the hopper walls, but since the amplitude is greater here than in prior values of Γ, there is an increased particle velocity at the first amplitude peak (light blue, Figure 12i). The same pattern is observed for the intrinsic excitation frequency peak (Figure 12k). The 300 Hz case (Figures 12m–n) displays the same results seen from the earlier simulations of the same frequency, and it is no longer discussed to save space.

TABLE 6 | Average flow rate comparison between monodisperse and bi-disperse cases at Γ = 6.

f (Hz)	*W* [monodisperse] (g/s)	*W* [bi-disperse] (g/s)
25	0.2067	0.2074
50	0.2606	0.2514
100	0.2801	0.2796

4.3.2 | Bi-disperse Case

A recognizable secondary frequency is still present in the bi-disperse cases. Comparing the mass flow rates for the two particle mixtures, an observed peculiarity reveals that the 25 Hz and 100 Hz cases are almost identical, but there is a difference of 8 mg/s between the monodisperse and bi-disperse cases (Table 6). Whilst the flow rates are comparatively similar given the small values, the difference implies that the conditions established

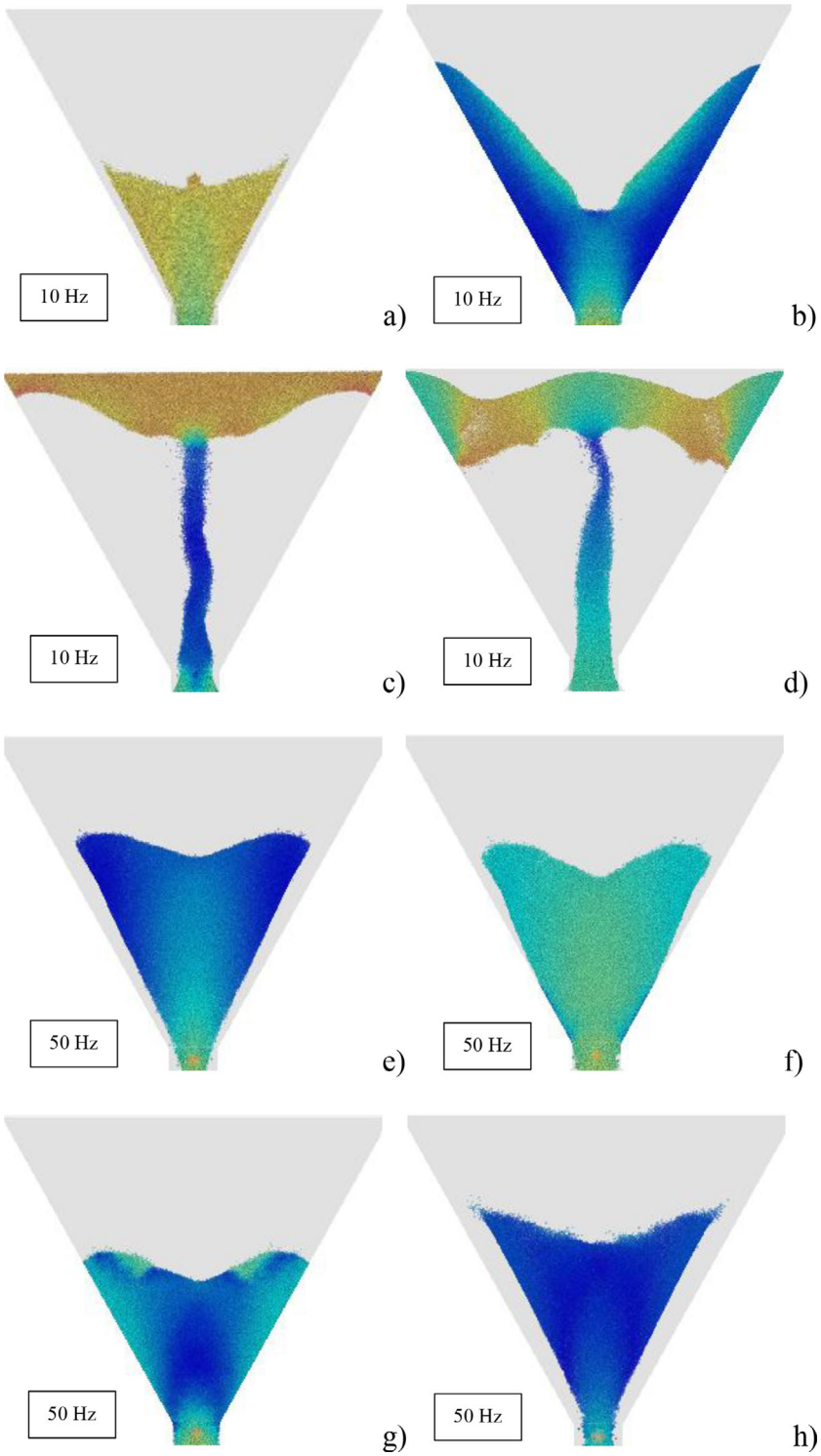

FIGURE 12 | Particle velocity contour maps for $\Gamma = 6$ (monodisperse case) and selected frequencies: (a) 10 Hz maximum velocity, main frequency, (b) 10 Hz minimum velocity, main frequency; (c) 10 Hz maximum velocity, secondary frequency; (d) 10 Hz minimum velocity, secondary frequency; (e) 50 Hz maximum discharge, main frequency; (f) 50 Hz minimum discharge, main frequency; (g) 50 Hz maximum discharge, secondary frequency; (h) 50 Hz minimum discharge, secondary frequency; (i) 100 Hz maximum discharge, main frequency; (j) 100 Hz minimum discharge, main frequency; (k) 100 Hz maximum discharge, secondary frequency' (l) 100 Hz minimum discharge, secondary frequency; (m) 300 Hz maximum discharge; (n) 300 Hz minimum discharge.

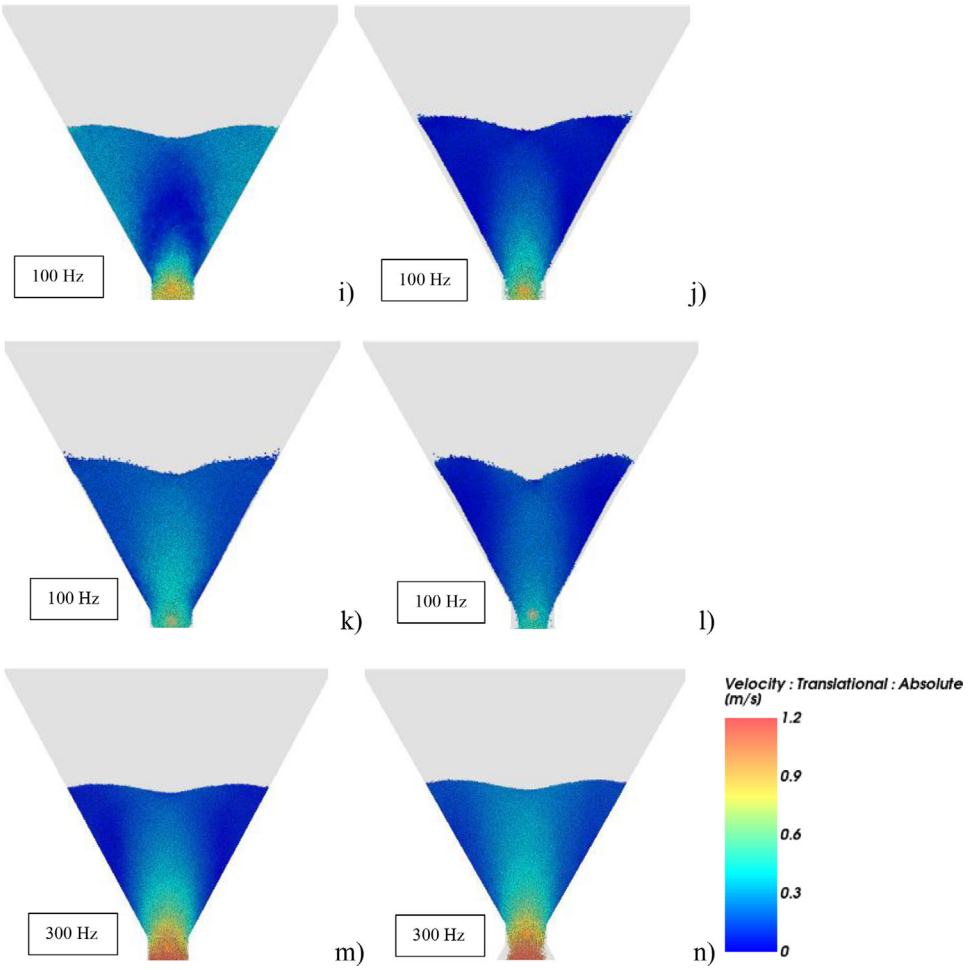

FIGURE 12 | (Continued)

in the material favor the monodisperse case, or the increased number of particles has a greater impact on the mass flow rate at 50 Hz than 25 Hz or 100 Hz.

This type of discrepancy does not appear for the $\Gamma = 2$ or $\Gamma = 4$ cases, which further suggests that the higher amplitude at $\Gamma = 6$ modifies the system response. The general response is similar for both flow types, and the trend line between 50–100 Hz implies that the bi-disperse case may supersede the monodisperse case at frequencies >100 Hz.

The corresponding flow patterns are qualitatively similar to those reported for the monodisperse case. At 25 Hz, high levels of shearing are experienced in the hopper, much like the $\Gamma = 2$ and $\Gamma = 4$ cases. Initially high particle flow can be seen in Figure 13a, with avalanching behavior once again present in Figure 13b. The bed separation occurs at the second local maximum (Figure 13c), with the particle velocities consistent between the first local maximum (Figure 13a) and minimum. At the second minimum (intrinsic excitation frequency, Figure 13d) the particle velocity has started to slow, with high levels of separation visible as the particles reach the top of the hopper. The 50 Hz and 100 Hz simulations are qualitatively similar to the monodisperse cases (Figures 13e–l).

4.4 | Frequency Spectrum Analysis

As already discussed to a certain extent in Sections. 4.1–4.3, in the $\Gamma = 4$ and $\Gamma = 6$ cases, "intrinsic" excitation frequencies were showing up in addition to that of the forcing (i.e., the imposed vibration frequency f). These cases, therefore, require additional analysis. A Fast Fourier Transform (FFT) has been performed accordingly to characterize more precisely these behaviors (Figures 14 and 15).

In particular, we begin the related discussion from the two prominent cases for $\Gamma = 4$, where, as mentioned in Sects. 4.2, an extra frequency was clearly present, namely, $f = 10$ Hz and 25 Hz. Interestingly, a closer analysis of the quantitative FFT outcomes reveals that at 10 Hz (Figure 14a), this secondary frequency is just a harmonic of the fundamental one (an integer multiple N of f with $N = 2$, i.e., 20 Hz); however, a set of incommensurate frequencies can also be identified (although their amplitude is clearly smaller than those of the fundamental frequency and its aforementioned harmonic), while the rest of the spectrum (for frequencies larger than 60 Hz) essentially displays low-amplitude noise. At 25 Hz (Figure 14b), there is a marked decrease in the amplitude of the secondary frequency (harmonic corresponding to $\cong 50$ Hz). Interestingly, incommensurate frequencies appear in

the range between 25 and 50 Hz having amplitudes comparable to the second harmonic.

Nevertheless, for f larger than 50 Hz, the amplitude of the harmonic $N = 2$ is almost negligible (Figure 14c,d) and the tendency to produce incommensurate frequencies is also strongly mitigated (incommensurate frequencies are scarcely recognizable or completely absent for these cases).

Notably, for $\Gamma = 6$, the situations becomes more complex as multiple peaks in addition to the imposed (vibration) one manifest over a wider range of frequencies.

More specifically, at 10 Hz (Figure 15a), the range of frequencies qualitatively aligns with that of the $\Gamma = 4$ case. Incommensurate frequencies can again be discerned in addition to the harmonic $N = 2$. Here, however, the $N = 2$ harmonic is even stronger.

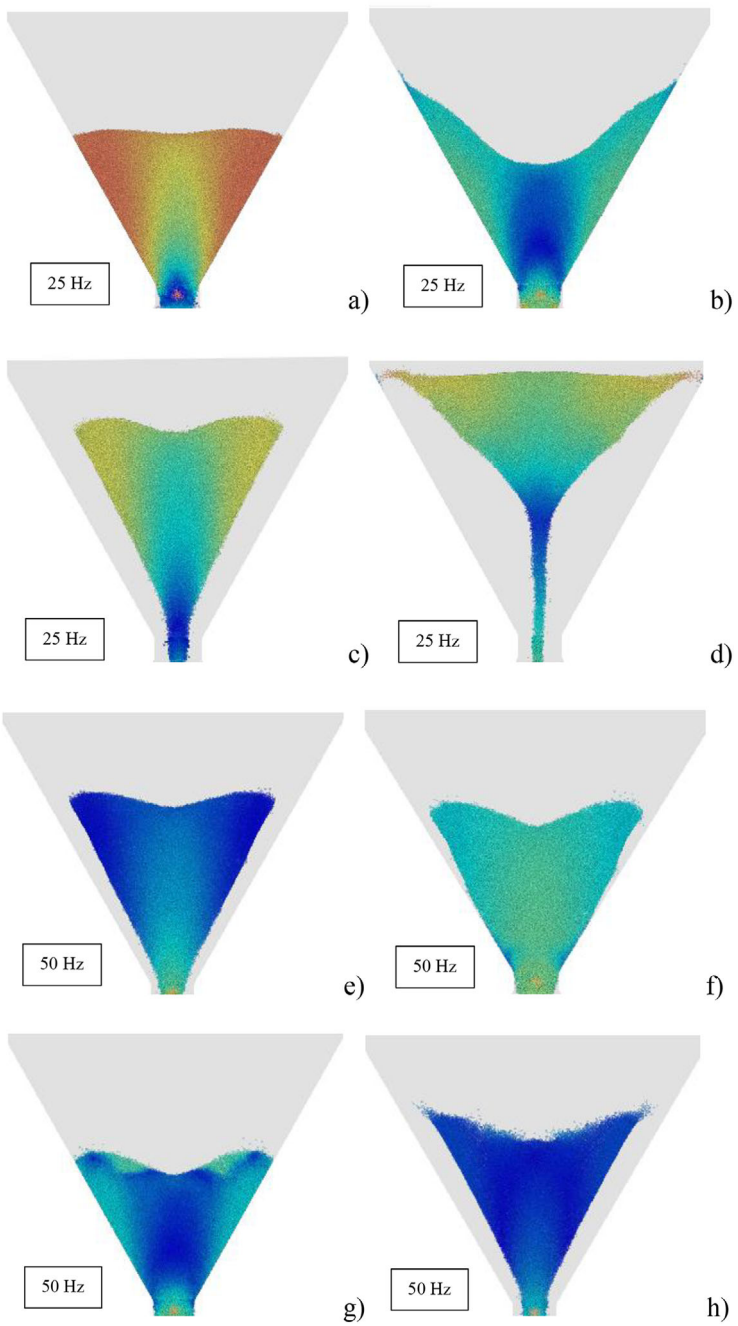

FIGURE 13 | Particle velocity contour maps for $\Gamma = 4$ (polydisperse case) and selected frequencies: (a) 25 Hz maximum discharge, main frequency; (b) 25 Hz minimum discharge, main frequency; (c) 25 Hz maximum discharge, secondary frequency; (d) 25 Hz minimum discharge, secondary frequency; (e) 50 Hz maximum discharge, main frequency; (f) 50 Hz minimum discharge, main frequency; (g) 50 Hz maximum discharge, secondary frequency; (h) 50 Hz minimum discharge, secondary frequency; (i) 100 Hz maximum discharge, main frequency; (j) 100 Hz minimum discharge, main frequency; (k) 100 Hz maximum discharge, secondary frequency; (l) 100 Hz minimum discharge, secondary frequency.

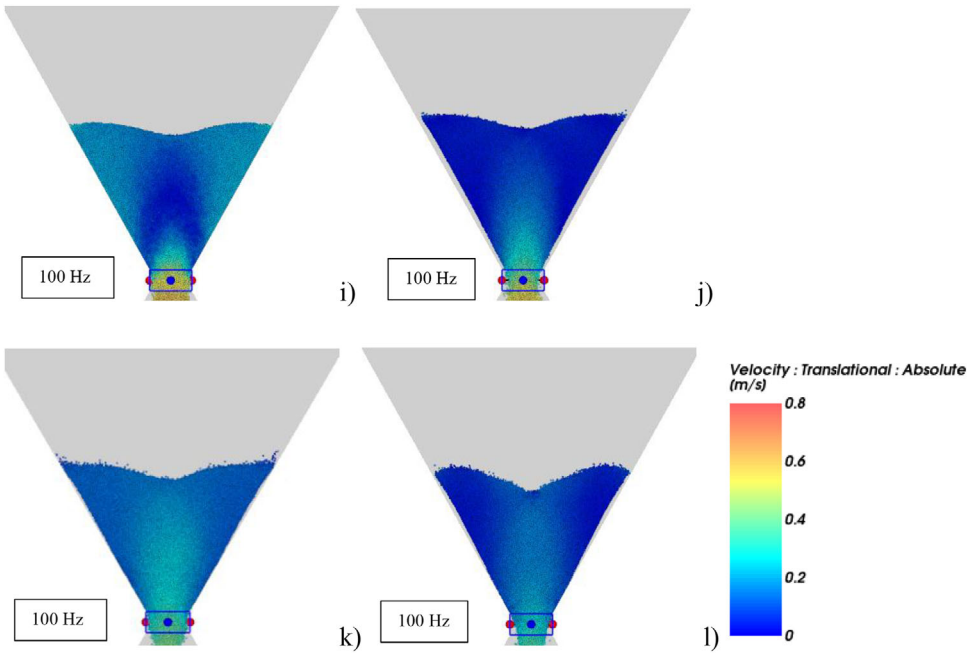

FIGURE 13 | (Continued)

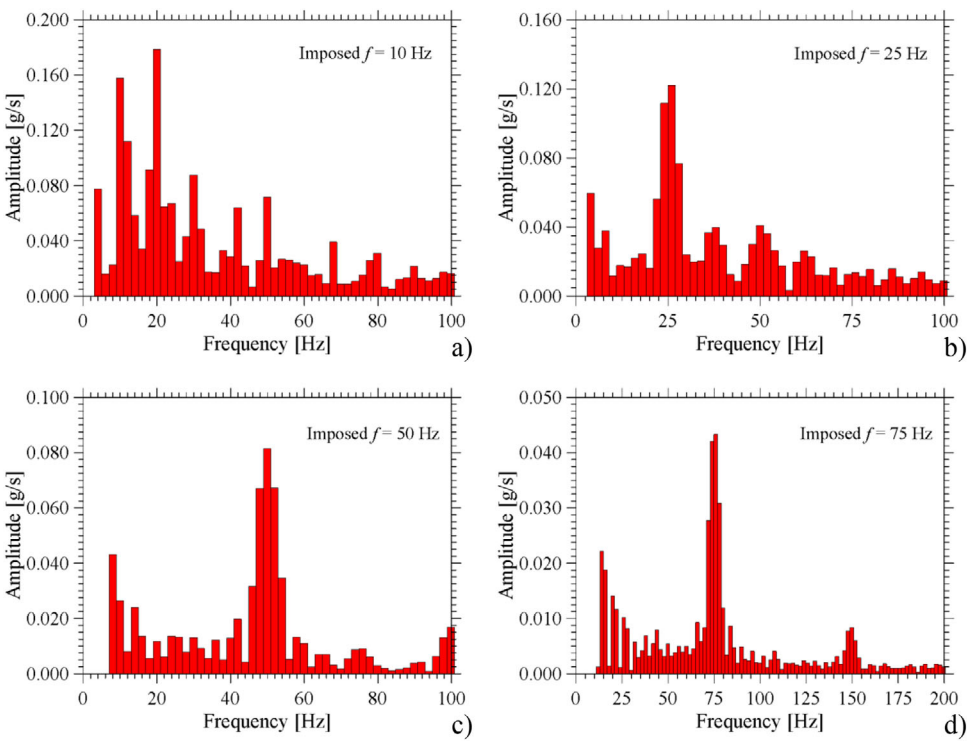

FIGURE 14 | Frequency spectra for $\Gamma = 4$: (a) 10 Hz, (b) 25 Hz, (c) 50 Hz, (d) 75 Hz.

Overall, the magnitude of the involved modes is significantly larger with respect to the corresponding situation (10 Hz) at $\Gamma = 4$.

At 25 Hz (Figure 15b), in addition to the fundamental frequency other (minor) peaks, all having the same amplitude, can be recognized at 50, 75 and 100 Hz (representing harmonics with $N = 2,3$ and 4, respectively); again incommensurate frequencies appear in the interval from 25 to 50 Hz having amplitude comparable to the harmonics; overall, in this case, the non-negligible modes span a much wider range of frequencies than that seen for the equivalent $\Gamma = 4$ case, and even for the 10 Hz simulation at $\Gamma = 6$.

At 50 Hz (Figure 15c), the major (largest amplitude) frequency occurs for the same value of the forcing (as expected), however, a

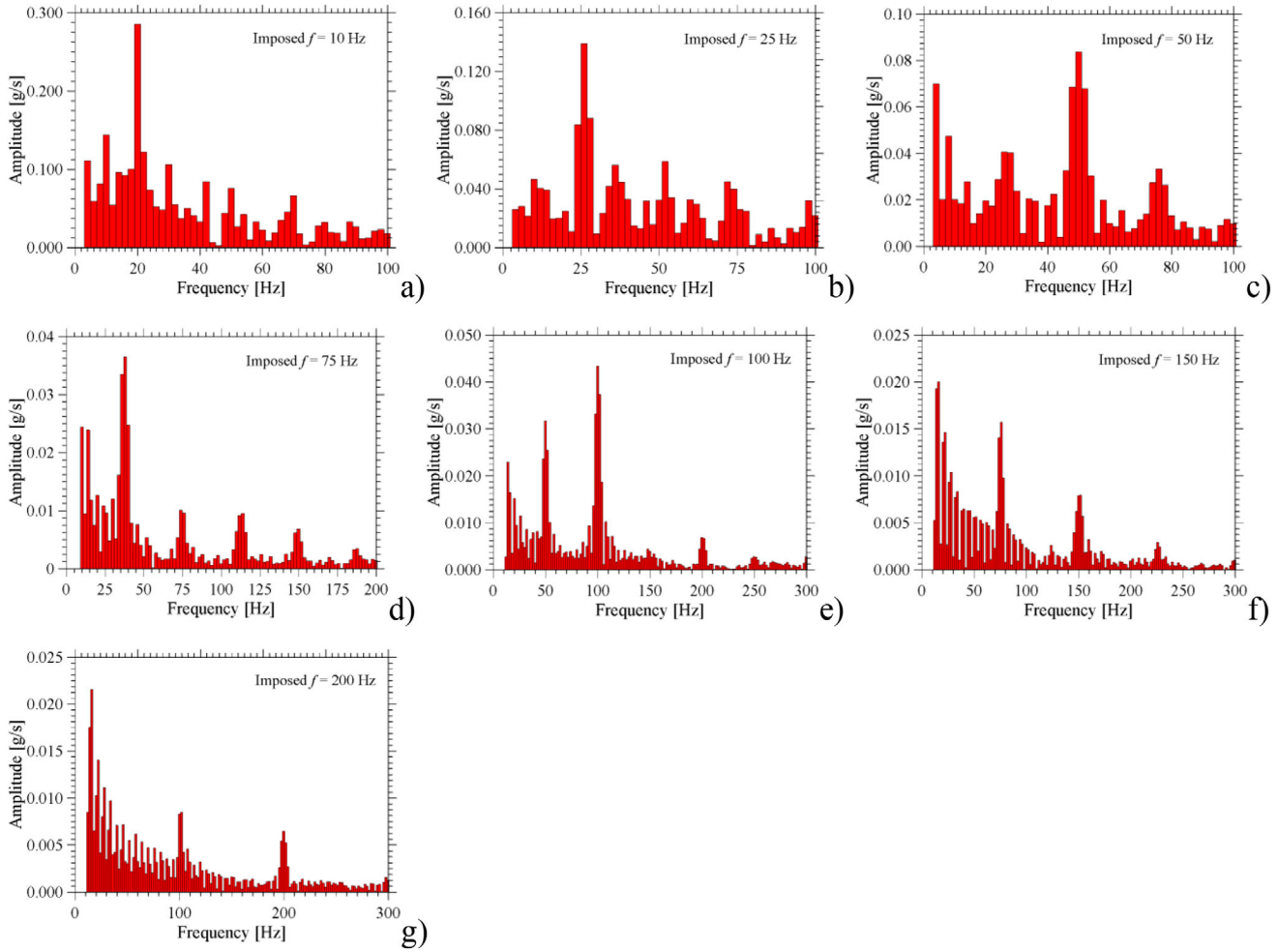

FIGURE 15 | Frequency spectra for Γ = 6: (a) 10 Hz, (b) 25 Hz, (c) 50 Hz, (d) 75 Hz, (e) 100 Hz, (f) 150 Hz, (g) 200 Hz.

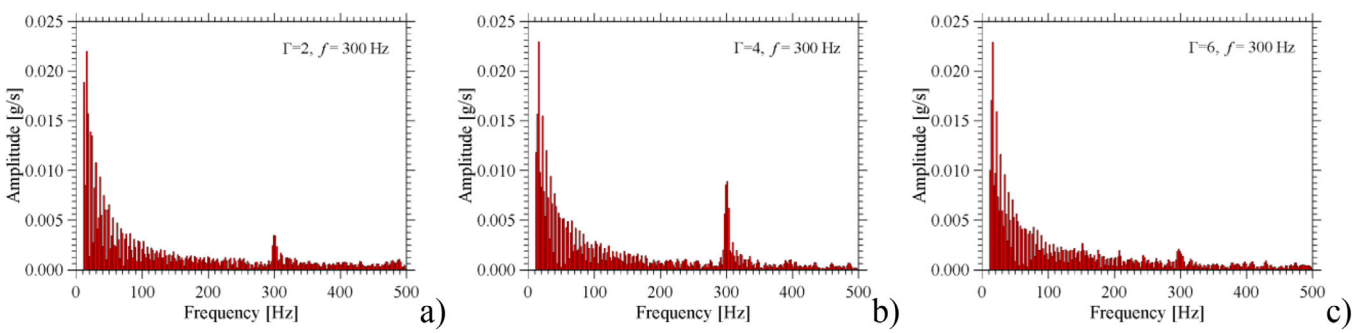

FIGURE 16 | Frequency spectra for a frequency of 300 Hz and various values of Γ: (a) Γ = 2, (b) Γ = 4, (c) Γ = 6.

subharmonic peak can be recognized at ≅25 Hz. The tendency of the system to generate subharmonics becomes even more evident for larger values of *f*, where the peaks of the subharmonics even exceed that of the forcing frequency (Figures 15d–g).

For completeness, we also present an FFT of the 300 Hz mass flow rate signals. In this respect, Figure 16 indicates that, at this frequency, regardless of the considered value of Γ, the typical features of a turbulent spectrum can be identified, with the amplitudes of the involved modes becoming progressively smaller as the frequency increases. While for Γ = 2 and Γ = 4 distinct peaks can still be clearly discerned at the forcing frequency, these are barely recognizable for Γ = 6, which indicates a clear tendency of the system to lose memory of the forcing as the driving force (Γ in our case) is increased, a behavior that is characteristic of fully developed turbulence.

In a turbulent spectrum the progressive decrease of amplitude with increasing frequency reflects how energy is transferred and dissipated across scales. Energy is typically injected at large scales, corresponding to low frequencies, where motions are coherent and carry most of the kinetic energy. Nonlinear

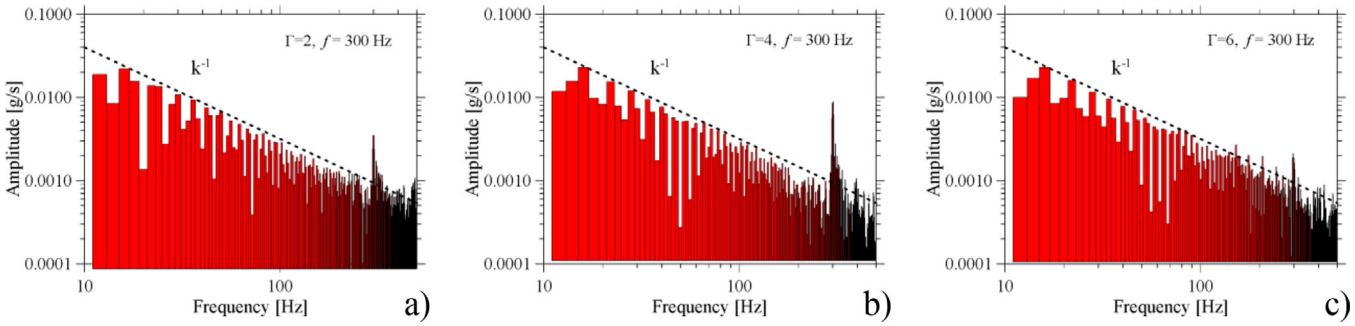

FIGURE 17 | Same data appearing in Figure 16 plotted in logarithm scale.

interactions then redistribute this energy toward smaller scales, spreading it over an increasing number of degrees of freedom, so the energy content associated with each scale diminishes. As frequency increases, viscous or collisional dissipation becomes increasingly effective, removing energy faster than it can be replenished by the cascade.

As a concluding remark for this section, it is also worth highlighting that the final turbulent states shown in Figure 16 stem from a situation in which harmonics, subharmonics and incommensurate frequencies, all contribute to determine the final behavior of the system; and, notably, additional insights into these states can be gathered from the spectra, if logarithm scaling is used for the axes. The significance of this alternate visualization (Figure 17) resides in its ability to make evident that the considered phenomena obey a k^{-1} scaling. Although it differs considerably from the well-known -5/3 scaling typical of the inertial range of self-similar isotropic (Kolmogorov) turbulence in fluids, similar scaling has been reported very recently by Yu et al. [100] in three-dimensional (3D) steady heap flow. These authors identified two distinct power spectrum regimes: one from the fast-flowing surface layer and another from the underlying creep layer, both exhibiting power-law spectra $\sim k^{-\alpha}$, with α ranging in the surface layer from 0.8 to 1.0 in agreement with the "running" sandpile model originally proposed by Hwa, and Kardar [101], which may regarded as a hint for possible future attempts to interpret the present results in the light of the same model.

5 | Discussion and Conclusion

5.1 | General Trends

In light of all the information and related quantitative details presented in Section 4, some general trends can be identified.

We have shown that the mass flow rate generally becomes higher as the frequency increases, reaching a plateau between 150 and 200 Hz. Beyond this, the flow rate remains approximately constant which, in line with the earlier findings by Wassgren et al. [102] and Suzuki et al. [103], confirms a limit of maximum flow rate exists. The mass flow rate is slightly higher for $\Gamma = 2$, reaching 0.329 g/s, whilst for $\Gamma = 4$ and 6, the mass flow rates are 0.319 and 0.313 g/s, respectively, which indicates it tends to decrease at higher values of Γ. Moreover, the larger the value of Γ, the higher the frequency to make the mass flow rate under the effect of vibrations larger than that induced by gravity only. The simplest way to justify this counterintuitive finding is via the increased inter-particle collisions [104, 105]. More precisely, the apparently paradoxical reduction of mass flow rate with increasing the dimensionless acceleration Γ can be understood by considering how vibrations modify the internal force network and shear resistance of granular materials rather than simply promoting bulk mobility.

At low to moderate vibration levels, oscillations help particles to rearrange, intermittently break force chains, and reduce static arching at the hopper outlet, thereby enhancing discharge relative to gravity-driven flow. However, as Γ grows, vibrations progressively dominate over gravity and induce a strongly agitated state in which particle contacts become more frequent but also more transient. Under these conditions, the material experiences an effective increase in internal shear resistance due to repeated collisions, enhanced dilation, and continual reformation of force chains with unfavorable orientations for downward flow. This interpretation is supported by existing studies in literature. Past experiments such as those by Knight et al. [34] and Philippe and Bideau [35] have clearly shown that vibrations can produce a compactification of the material, that is, an increase in the density starting from an initially smaller value. Studies such as these have produced densification curves well fitted by a stretched exponential with the characteristic time of compaction following an Arrhenius relation where the dimensionless acceleration Γ plays the role of temperature. Along the same lines, shear tests reported by Schellart [104] have confirmed that granular materials subjected to cyclic or dynamic loading can exhibit increased effective friction and apparent cohesion due to contact interlocking and fabric anisotropy, effects that scale with agitation intensity and particle angularity [104].

Moreover, at high Γ values the granular bed tends to partially fluidize and lose sustained contact with the hopper walls and outlet region during parts of the vibration cycle. This reduces the mean normal stress driving discharge, since gravity no longer acts continuously on a quasi-static column of material. As a consequence, the average mass flow rate decreases, and a higher vibration frequency is required to re-establish conditions in which vibrations assist rather than hinder flow. This frequency threshold corresponds to the point at which vibration-induced rearrangements occur rapidly enough to prevent long-lived arches while still maintaining sufficient contact forces to transmit weight to the outlet. These effects are further amplified in materials with high angularity and friction, such as lunar regolith and its simulants. As discussed by Jayathilake et al. [105], angular

grains exhibit stronger interlocking and higher shear strength, making them particularly sensitive to vibration-induced changes in contact mechanics. In such materials, increasing Γ intensifies collisional dissipation and frictional losses, so that vibrations only become beneficial above a critical frequency where arch disruption outweighs the adverse effects of reduced effective loading and enhanced shear resistance.

Other identified general trends concern the frequency spectrum. Overall, the effect of increasing Γ at fixed f can be clearly identified through a cross-comparison of Figures 3, 7, and 11. Moreover, the dedicated FFT analysis presented in Section 4.4 has revealed an increase in complexity for higher imposed vibration frequency f and/or higher Γ itself. For a fixed value of Γ, increasing f typically leads to the appearance of higher-order harmonics, namely integer multiples of f. These are clearly visible, for example, in Figures 14 and 15. The frequency-spectrum analysis has further shown that, upon a continued increase in the forcing frequency at fixed Γ, sub-harmonic frequencies appear in the spectrum. This behavior is particularly evident for $\Gamma = 6$, as illustrated in Figure 15.

The existence of subharmonics and related period doubling bifurcation is not a new finding in the field of vibrated granular matter [37, 106, 107]. When a granular layer is vertically vibrated with sufficient acceleration to exceed gravity, the material undergoes repeated phases of detachment, free flight, and impact with the vibrating container. Energy is injected during contact with the container but dissipated during collisions and internal rearrangements. Because dissipation is strong, the state of the system after one forcing cycle is generally not identical to its state at the beginning of that cycle. Compaction, dilation, and re-organization of force chains introduce a form of mechanical memory. As a result, the granular material may require two driving periods to return to a dynamically equivalent configuration. This loss of invariance under time translation by one period manifests as a stable response with twice the driving period, corresponding to a sub-harmonic at half the forcing frequency.

In other words, from a dynamical systems perspective, the vibrated granular mass behaves like a driven, dissipative nonlinear oscillator described effectively by a discrete map sampled once per forcing cycle. As control parameters such as vibration amplitude or frequency are increased, a stable period-one orbit can lose stability through a period-doubling bifurcation, giving rise to period-two motion and, consequently, a spectral peak at the sub-harmonic frequency. Higher-order subharmonics may emerge through further bifurcations as the system approaches chaotic dynamics.

It is also worth highlighting that, physically, these subharmonics represent collective modes of the granular assembly rather than oscillations of individual grains. They reflect coherent, layer-scale motion in which impacts, compaction, and energy dissipation alternate from cycle to cycle. In this sense, the presence of subharmonics is a direct spectral signature of broken temporal symmetry and nonlinear self-organization in vibrated granular matter.

The emergence of the aforementioned incommensurate frequencies for relatively low values of f and moderate values of Γ also deserves some attention and physical reasoning as further discussed in the next Section 5.2.

5.2 | Incommensurate Frequencies

In terms of frequency spectra, as already outlined in Section 4.4, another key observation concerns the lower portion of the frequency range, where complex dynamical responses can arise even before the excitation of the aforementioned subharmonics. Indeed, we have found that even for $\Gamma = 4$, the spectrum can already exhibit substantial complexity, including frequencies incommensurate with the forcing, at values as low as 10 Hz.

The emergence of incommensurate frequencies at relatively low forcing frequencies, such as 10–25 Hz, can be explained by the intrinsically nonlinear and multi-scale nature of vibrated granular systems, especially when frictional and geometric constraints are strong [108–112]. More specifically, at low forcing frequencies, the imposed vibration period becomes comparable to the characteristic timescales of internal granular rearrangements, including contact formation and breakage, force-chain evolution, and intermittent stick–slip motion at particle contacts and against the hopper walls. In this regime, the granular assembly does not respond as a simple periodically forced system. Instead, it develops its own internal dynamics, which are governed by collective rearrangement events rather than by the external excitation alone. These internally generated timescales are generally not integer multiples of the forcing period, leading to the appearance of incommensurate frequencies in the spectrum.

This effect is further enhanced by particle angularity and friction. Angular grains promote interlocking and the formation of metastable structures that persist over several vibration cycles before collapsing abruptly. The collapse and reformation of these structures occur intermittently and irregularly, introducing characteristic frequencies associated with episodic yielding or localized shear events. Because these processes are controlled by evolving contact networks rather than by the imposed vibration, their spectral signatures are not harmonically related to the forcing frequency.

This interpretation is strongly supported by DEM studies on nonspherical granular assemblies. Walton and Johnson [113] demonstrated that angular and clustered particle representations of lunar regolith significantly enhance shear resistance through geometric interlocking, leading to the emergence of more stable and persistent contact configurations compared with spherical particles. Their results show that particle shape governs the stability and longevity of force chains, which in turn control the system's ability to sustain load-bearing structures under dynamic conditions. In this context, metastable configurations arise naturally from the enhanced geometric constraints imposed by angular grains, and their sudden breakdown corresponds to the reorganization of these strongly anisotropic force networks. Similarly, Zhang and Makse [114] showed that frictional granular systems exhibit a jamming transition characterized by long-lived metastable states separated by abrupt rearrangements. These states are stabilized by friction-induced force chains and persist until external perturbations or internal stress accumulation trigger sudden unjamming events. The resulting dynamics are

inherently intermittent and history-dependent, with transitions between mechanically stable configurations occurring in a non-periodic manner. This framework provides a direct physical basis for interpreting the observed episodic yielding in terms of transitions between jammed and unjammed states of the evolving contact network and ensuing non-periodic system response.

Additionally, at low frequencies the system experiences quasi-static loading and unloading during each vibration cycle. During the slow phases of the oscillation, the granular bed can partially relax under gravity, while during acceleration phases it can undergo dilation and loss of contact. The alternation between these states leads to nonlinear mode coupling and to a competition between gravity-driven relaxation and vibration-induced mobilization. As shown in studies of frictional and shape-dependent granular packings (see again Walton and Johnson [113]), the presence of angular particles further amplifies this competition by stabilizing transient force-chain networks, thereby increasing the residence time of metastable configurations. Within the jamming framework proposed by Zhang and Makse [114], this behavior can be interpreted as repeated transitions between metastable jammed states driven by slowly varying stress conditions. As a result, the system response is governed primarily by internal relaxation and structural reorganization timescales rather than by the external forcing frequency, leading to a broadband and non-harmonically related spectral signature.

As a concluding remark for this section, it is also worth highlighting that the final turbulent states shown in Figure 16 stem from a situation in which harmonics, subharmonics and incommensurate frequencies, all contribute to determine the final behavior of the system.

Having summarized the main trends of the considered system together with related possible interpretations based on the existing literature, we turn now to discussing such findings in relation to ISRU-related concepts (Section 5.3).

5.3 | ISRU Relevance

For ISRU activities, in general, the emphasis is on accurate and repeatable dispensing of regolith. Hence the observations elaborated in Sects. 5.1 and 5.2 allow the derivation of potentially useful indications. As a first example, it becomes immediately evident that, given above-mentioned phenomena, low-frequencies for fixed values of Γ would be unsuitable for material processing due to the related intrinsic unpredictability of the mass flow.

From the simulations carried out in this study, the considered material would discharge consistently and at a maximum between 50–300 Hz. As the value of Γ increases, it requires an increasingly higher frequency to produce the desired effects of W_d>1. This suggests that experimenting with values of Γ>6 would not be beneficial, as the amplitude increase would create material rebounding and inter-particle collisions. A table is provided below which indicates the interpolated frequency value at which W_d>1 for each value of Γ (Table 7).

For frequencies less than ≈75 Hz, both Γ = 4 and Γ = 6 discharge at less than that of purely gravitational flow. Γ = 6 does not provide an increase in mass flow rate up to ≈125 Hz. By contrast, at Γ = 2, the mass flow rate is noticeably improved with respect to the purely gravitational discharge even at frequencies <50 Hz. On the basis of all these arguments, it can therefore be concluded that the mass flow rate of the considered material is generally an improvement upon a purely gravity-driven flow when the frequency is high, provided the amplitude remains relatively low. Moreover, very low frequencies should be avoided not only because they do not lead to any advantage with respect to the corresponding purely gravitational flow, but also because they may even cause detrimental effects in terms of spurious frequencies excitation and ensuing unpredictable response of the flow.

TABLE 7 | Frequencies at which the dimensionless discharge is above 1 (W_d>1).

Γ = 2	Γ = 4	Γ = 6
38.5 Hz	70.8 Hz	120.7 Hz

5.4 | Flow Patterning Behavior

Other relevant arguments can be derived directly from a critical analysis of the flow patterning behavior itself.

Material clumping was present in some simulations. This was especially noted at lower frequencies, where the regolith continuum would remain together even. In particular, according to the present simulations, in the upper chamber of the hopper, the particles tend to aggregate together. After discharging through the orifice, the material also tends to remain as a continuum in the lower chamber. The particle mass breaks apart at high amplitudes and when passing through the orifice, and for high amplitudes this could lead to particles re-entering the orifice. An example of the mass breaking apart can be seen in the results section Figures 9a and 12a for 10 Hz for Γ = 4 and Γ = 6, respectively. By 25 Hz the particles tend to remain mostly as an entire continuum. Notably, these results indicate that the regolith's irregular shape significantly impacts the apparent cohesiveness, as also argued by Walton et al. [77] and Huang and Zheng [111].

As explained in Sect. 3.2, in the present study, regolith particles were created to emulate an irregular sphero-polyhedron morphology that would promote mechanical interlocking during agitation. Indeed, as mentioned above, the material has displayed an apparent cohesiveness, especially in the upper hopper chamber, where a pseudo-boundary layer of particles forms closest to the hopper wall. This has been observed at various frequencies, where the particles closest to the wall resist the hopper motion. The regolith tends to agglomerate, even at high amplitudes.

At all frequencies, the material has revealed shearing behavior. This was particularly noticeable at high amplitude, low-frequency simulations. As previously reported by [104], the particle size and irregular shape contribute to mechanical interlocking. In particular, in our simulations the shearing was very evident during the discharge oscillation cycle, where the discharge was at its maximum. The related mechanism can be depicted as follows: The center of the regolith mass moves at a

slower velocity as the hopper moves up. During the minimum part of the discharge cycle, the hopper moves downwards, the center column of particles begins to discharge in a funnel flow manner, whilst at the walls the particles remain slow, occasionally at high angles of repose, and with some small cusp-point formations (localized ratholing behavior) observable.

Moreover, as demonstrated by Fig. 13ab, although shearing is present in all frequency samples, at the lowest frequencies (10 Hz, 25 Hz), the particles become a discontinuous media. Hence high amplitude discharging hoppers can generate shearing forces capable of causing the regolith simulant to develop properties akin to a fluidized bed, but in the absence of air-blown devices. High particle velocities can be seen at low frequencies during the maximum part of the oscillation cycle, and likewise very slow velocities at the minimum point.

As the frequency tends towards infinity, funnel flow becomes dominant. This applies to all frequencies and Γ values but is most apparent at the 100 Hz and 300 Hz examples described in Section 4. It should be noted, however, that this observation should not be interpreted as evidence that funnel flow necessarily represents the asymptotic behavior in the limit of infinitely large frequencies. Previous DEM studies of wave propagation in granular media (e.g., Ning and Evans [115]) have shown that granular assemblies increasingly attenuate high-frequency disturbances, behaving effectively as a low-pass filter. Accordingly, once the excitation frequency exceeds the characteristic response frequencies of the granular bed, further increases in frequency may have only a limited influence on the bulk dynamics because a significant fraction of the imposed energy is dissipated through the evolving contact network. The similarity observed between the highest-frequency cases considered here may therefore reflect such scenario.

For some frequencies, we have also found a tendency to "avalanching." This occurs when the wall-bound, slow-moving particles exceed the regolith's angle of repose and travel towards the center of the mass. This is another feature of funnel flow, and it indicates the hopper walls were not shallow enough to allow for a mass flow regime. In particular, from the sampled flow pattern frequencies, 300 Hz provides the most consistent flow behavior. This is due to 300 Hz corresponding to a low amplitude for all values of Γ.

5.5 | Conclusions and Future Directions

The study presented here provides initial insights into the numerically simulated response of vibrated granular materials, specifically lunar regolith simulants, flowing through a hopper. The model has proven able to capture several qualitative features observed in experimental studies [29], such as the influence of vertical vibrations on flow regularity, reduction of jamming probability, and the emergence of distinct flow regimes including funnel, mass, and ratholing patterns.

Remarkably, the numerical simulations have satisfactorily reproduced the general trend where low-frequency vibrations promote arching due to insufficient energy to break force chains, while higher-frequency excitations can both facilitate flow and, under certain conditions, induce intermittent clogging. These qualitative agreements demonstrate that the current numerical framework can provide a useful starting point for exploring the dynamic behavior of granular assemblies under vibration.

However, the model remains at an early stage of development. The present simulations have employed a simplified representation of particle shapes and size distributions. While nonspherical particles have been included to capture angularity effects, only a limited number of size classes have been considered, and the particle polydispersity is far from the heterogeneous distributions observed in experimental lunar regolith simulants. This simplification limits the ability of the model to fully reproduce the spatio-temporal patterns of material displacement, the formation and collapse of force chains, and the more complex frequency-dependent flow phenomena observed in experiments. For example, the onset of incommensurate frequencies and the re-emergence of clogging at high frequency and low amplitude are strongly influenced by polydispersity and angularity, suggesting that the current model may underestimate or misrepresent these effects.

Further evidence for the need for more sophisticated representations is provided by the observation that the results obtained with the bi-disperse population are nearly indistinguishable from those of the monodisperse case. This clearly indicates that a 10% variation in mass and a particle size difference of only 30% are insufficient to induce meaningful microstructural changes in the packing.

Future numerical work should therefore incorporate more realistic multi-disperse particle distributions, including broader size spectra and improved representations of particle angularity and roughness. This would allow the model to better capture interlocking, dilation, and local rearrangement dynamics, thereby producing flow behavior that more closely matches experimental findings. Additionally, systematic variation of vibration parameters in combination with enhanced particle realism would provide the opportunity to explore thresholds for arch formation and the transitions between flow regimes with greater fidelity.

Author Contributions

L.T. conducted the required numerical simulations, prepared all the figures showing the particle distribution, and provided a detailed description of the results. He also made substantial contributions to the literature review. P.W. contributed to setting up the numerical simulations. S.V.B. contributed to the literature review and supervised P.W. A.A. contributed to the description of the mathematical model. M.L. (P.W.'s and L.T.'s supervisor) interpreted the results in light of the existing literature, developed relevant analogies with other nonlinear systems, and wrote the main manuscript text. All authors reviewed and approved the manuscript.

Funding

This work has been financially supported by the European Space Agency, ESA Contract 4000138607/22/NL/GLC/my, the Open Space Innovation Platform (OSIP). The authors also wish to acknowledge the support of EPSRC for contributing to the PhD scholarship of P. Watson and the Advanced Forming Research Centre (AFRC) within the National Manufacturing Institute Scotland (NMIS) for contributing to the PhD scholarship of L. Traquair.

Data Availability Statement

The data that support the findings of this study are openly available in Pure at https://doi.org/10.15129/3496fd41-17d1-42ac-b5db-be9974921922.

References

1. European Space Agency, "ESA Strategies for Science at the Moon," 1992, European Space Agency, ESA Report.

2. G. B. Sanders, K. A. Romig, and W. E. Larson, "Results from the NASA Capability Roadmap Team for in-situ Resource Utilization (ISRU)," in International Lunar Conference (2005), 2005 (No. KSC-2005-116).

3. D. L. Linne, G. B. Sanders, S. O. Starr, et al. Overview of NASA Technology Development for in-situ Resource Utilization (ISRU) (2017). In International Astronautical Congress (No. GRC-E-DAA-TN46532).

4. A. Makaya, L. Pambaguian, T. Ghidini, T. Rohr, U. Lafont, and A. Meurisse, "Towards out of Earth Manufacturing: Overview of the ESA Materials and Processes Activities on Manufacturing in Space," *CEAS Space Journal* 15, no. 1 (2023): 69–75, https://doi.org/10.1007/s12567-022-00428-1.

5. D. S. McKay, G. Heiken, A. Basu, et al., "Lunar Regolith," *Lunar sourcebook* 567 (1991): 285–356.

6. J. Venkatraman, T. Horvath, T. M. Powell, and D. A. Paige, "Statistical Estimates of Rock-free Lunar Regolith Thickness from Diviner," *Planetary and Space Science* 229 (2023): 105662, https://doi.org/10.1016/j.pss.2023.105662.

7. A. Ellery, "Sustainable in-situ Resource Utilization on the Moon," *Planetary and Space Science* 184, no. 1 (2020): 105662, https://doi.org/10.1016/j.pss.2020.104870, Article.

8. M. Anand, I. A. Crawford, M. Balat-Pichelin, et al., "A Brief Review of Chemical and Mineralogical Resources on the Moon and Likely Initial in Situ Resource Utilization (ISRU) Applications," *Planetary and Space Science* 74, no. 1 (2012): 42–48, https://doi.org/10.1016/j.pss.2012.08.012.

9. K. L. Ferrone, A. B. Taylor, and H. Helvajian, "In Situ Resource Utilization of Structural Material from Planetary Regolith," *Advances in Space Research* 69, no. 5 (2022): 2268–2282, https://doi.org/10.1016/j.asr.2021.12.025.

10. W. Carrier III, J. K. Mitchell, and A. Mahmood, "The Nature of Lunar Soil," *Journal of the Soil Mechanics and Foundations Division* 99, no. 10 (1973): 813–832, https://doi.org/10.1061/JSFEAQ.0001935.

11. G. Heiken, D. Vaniman, and B. M. French, *Lunar Sourcebook: A User's Guide to the Moon* (Cambridge University Press, 1991).

12. J. Connolly and W. D. Carrier, "An Engineering Guide to Lunar Geotechnical Properties," in 2023 IEEE Aerospace Conference (IEEE, 2023), 1–9.

13. O. R. Walton, "Challenges in Transporting, Handling and Processing Regolith in the Lunar environment," in *Moon: Prospective Energy and Material Resources* (2012), 267–293.

14. H. Landry, E. Piron, J. M. Agnew, C. Lague, and M. Roberge, "Performance of Conveying Systems for Manure Spreaders and Effects of Hopper Geometry on Output Flow," *Applied engineering in agriculture* 21, no. 2 (2005): 159–166, https://doi.org/10.13031/2013.18147.

15. A. N. Faqih, A. W. Alexander, F. J. Muzzio, and M. S. Tomassone, "A Method for Predicting Hopper Flow Characteristics of Pharmaceutical Powders," *Chemical Engineering Science* 62, no. 5 (2007): 1536–1542, https://doi.org/10.1016/j.ces.2006.06.027.

16. R. O. Uñac, A. M. Vidales, O. A. Benegas, and I. Ippolito, "Experimental Study of Discharge Rate Fluctuations in a Silo with Different Hopper Geometries," *Powder technology* 225 (2012): 214–220, https://doi.org/10.1016/j.powtec.2012.04.013.

17. E. Rojas, V. Vergara, and R. Soto, "Case Study: Discrete Element Modeling of Wear in Mining Hoppers," *Wear* 430 (2019): 120–125, https://doi.org/10.1016/j.wear.2019.04.020.

18. J. J. Fitzpatrick, S. A. Barringer, and T. Iqbal, "Flow Property Measurement of Food Powders and Sensitivity of Jenike's Hopper Design Methodology to the Measured Values," *Journal of Food Engineering* 61, no. 3 (2004): 399–405, https://doi.org/10.1016/S0260-8774(03)00147-X.

19. J. N. Zatsarinnaya, A. G. Logacheva, and A. A. Solovyova, "Analysis of Thermodynamic Efficiency of the Fuel Preparation Systems with an Intermediate Hopper at Thermal Power Plants," in IOP Conference Series. *Earth and Environmental Science* (IOP Publishing, 2019).

20. Q. He, D. M. Du, Y. Wang, and Z. R. He, "Three-Dimensional Discrete Element Simulations of Round Hopper in Thermal Power Plant," *Applied Mechanics and Materials* 157 (2012): 45–48, https://doi.org/10.4028/www.scientific.net/AMM.157-158.45.

21. D. K. Chaturvedi and D. N. Tripathi, "Automatic Separation of Municipal Waste Using PLC and Smart Hopper," *International Research Journal of Engineering and Technology (IRJET)* 6, no. 03 (2019): 2395–0056.

22. J. Horabik and M. Molenda, "Mechanical Properties of Granular Materials and Their Impact on Load Distribution in Silos, a Review," *Scientia Agriculturae Bohemica* 45 (2014): 203–211, https://doi.org/10.1515/sab-2015-0001.

23. A. Rosato, D. Blackmore, N. Zhang, and Y. Lan, "A Perspective on Vibration-induced Size Segregation of Granular Materials," *Chemical Engineering Science* 57 (2002): 265–275, https://doi.org/10.1016/S0009-2509(01)00380-3.

24. Y. Yang, L. Liu, X. Li, et al., "Aerodynamic Grain-size Distribution of Blown Sand," *Sedimentology* 66 (2019): 590–603.

25. L. H. Lee, "Adhesion and Cohesion Mechanisms of Lunar Dust on the Moon's Surface," *Journal of Adhesion Science and Technology* 9 (1995): 1103–1124, https://doi.org/10.1111/sed.12497.

26. H. A. Perko, J. D. Nelson, and W. Z. Sadeh, "Surface Cleanliness Effect on Lunar Soil Shear Strength," *Journal of Geotechnical and Geoenvironmental Engineering* 127, no. 4 (2001): 371–383, https://doi.org/10.1061/(ASCE)1090-0241(2001)127:4(371).

27. B. Dotson, D. S. Valencia, C. Millwater, et al., "Cohesion and Shear Strength of Compacted Lunar and Martian Regolith Simulants," *Icarus* 411 (2024): 115943, https://doi.org/10.1016/j.icarus.2024.115943.

28. H. Kawamoto, "Vibration Transport of Lunar Regolith for in Situ Resource Utilization Using Piezoelectric Actuators," *Journal of Aerospace Engineering* 3 (2020): 04020014, https://doi.org/10.1061/(ASCE)AS.1943-5525.0001128.

29. M. Lappa, P. Watson, and S. Vincent-Bonnieu, "Vibrationally-aided Flow of Lunar Regolith Simulants in a Hopper-based Conveying Device," *Journal of Rheology* 70, no. 3 (2026): 557–579, https://doi.org/10.1122/8.0001055.

30. V. Nayagam and K. R. Sacksteder, "A Vibrofluidized Reactor for Resource Extraction from Lunar Regolith," *AIP Conference Proceedings* 813 (2006): 141–148.

31. D. Schulze, *Powders and Bulk Solids—Behavior, Characterization, Storage and Flow* (Springer, 2021).

32. M. Lappa, "New Methods for the Transport and Management of Lunar regolith," in *Why Space? The Opportunity for Material Science and Innovation*, UKRI-STFC and the Satellite Applications Catapult (2024), 131–133.

33. C. McKenzie, P. Watson, S. Vincent Bonnieu, and M. Lappa, "The Response of Lunar Regolith Simulants of Varying Particle Size Ranges to Vertical and Horizontal Vibrations," *Journal of Rheology* 70, no. 3 (2026): 533–556, https://doi.org/10.1122/8.0001041.

34. J. B. Knight, C. G. Fandrich, C. N. Lau, H. M. Jaeger, and S. R. Nagel, "Density Relaxation in a Vibrated Granular Material," *Physical review E* 51, no. 5 (1995): 3957, https://doi.org/10.1103/PhysRevE.51.3957.

35. P. Philippe and D. Bideau, "Compaction Dynamics of a Granular Medium under Vertical Tapping," *EPL (Europhysics Letters)* 60, no. 5 (2002): 677–683.

36. P. Watson, S. Vincent-Bonnieu, and M. Lappa, "Fluidization and Transport of Vibrated Granular Matter," *Fluid Dynamics and Materials Processing* 20 (2024): 1–29, https://doi.org/10.32604/fdmp.2023.029280.

37. P. Watson, S. V. Bonnieu, A. Anwar, and M. Lappa, "3D Waveforms and Patterning Behavior in Thin Monodisperse and Multi-disperse Vertically-Vibrated Layers," *Granular Matter* 27, no. 1 (2025): 19, https://doi.org/10.1007/s10035-024-01488-2.

38. M. Jiang, Z. Shen, and C. Thornton, "Microscopic Contact Model of Lunar Regolith for High Efficiency Discrete Element Analyses," *Computers and Geotechnics* 54 (2013): 104–116, https://doi.org/10.1016/j.compgeo.2013.07.006.

39. T. Liu, J. Zhou, L. Liang, Y. Zhao, and D. Cao, "Investigation of Effect of Stones on Lunar Regolith Drilling Using DEM," *Computers and Geotechnics* 131 (2021): 103958, https://doi.org/10.1016/j.compgeo.2020.103958.

40. M. Jiang, Z. Y. Yin, and Z. Shen, "Shear Band Formation in Lunar Regolith by Discrete Element Analyses," *Granular Matter* 18, no. 2 (2016): 32, https://doi.org/10.1007/s10035-016-0635-z.

41. H. Otto, K. Kerst, C. Roloff, G. Janiga, and A. Katterfeld, "CFD–DEM Simulation and Experimental Investigation of the Flow Behavior of Lunar Regolith JSC-1A," *Particuology* 40 (2018): 34–43, https://doi.org/10.1016/j.partic.2017.12.003.

42. B. Xi, M. Jiang, and L. Cui, "3D DEM Analysis of Soil Excavation Test on Lunar Regolith Simulant," *Granular Matter* 23, no. 1 (2021): 1, https://doi.org/10.1007/s10035-020-01070-6.

43. T. Liu, J. Zhou, L. Liang, Z. Bai, and Y. Zhao, "A Systematic Calibration and Validating Method for Lunar Soil DEM Model," *Advances in Space Research* 68, no. 9 (2021): 3925–3942, https://doi.org/10.1016/j.asr.2021.06.050.

44. M. Jiang, T. Zhao, and X. Wang, "DEM Modelling of Cone Penetration Tests in Lunar Soil," *Granular Matter* 24, no. 1 (2022): 5, https://doi.org/10.1007/s10035-021-01142-1.

45. B. Xi, M. Jiang, P. Mo, X. Liu, and J. Yang, "3D DEM Analysis of the Bearing Behavior of Lunar Soil Simulant under Different Loading Plates," *Granular Matter* 25, no. 4 (2023): 72, https://doi.org/10.1007/s10035-023-01355-6.

46. P. Młynarczyk, A. Kolusz, and A. Gallina, "Sensitivity Analysis of the DEM Model Numerical Parameters on the Value of the Angle of Repose of Lunar Regolith Analogs," *Artificial Satellites* 58 (2023): 188–202, https://doi.org/10.2478/arsa-2023-0022.

47. N. Zhou, J. Chen, N. Tian, K. Tian, J. Huang, and P. Wu, "Calibration of Discrete Element Method Parameters for a High-fidelity Lunar Regolith Simulant Considering the Effects of Realistic Particle Shape," *Materials* 17, no. 19 (2024): 4789, https://doi.org/10.3390/ma17194789.

48. I. P. Madden, S. Muruganandam, A. Missaoui, et al., "Behaviors of Lunar Regolith Simulants under Varying Gravitational Conditions," *Microgravity* 11, no. 1 (2025): 69, https://doi.org/10.1038/s41526-025-00501-z.

49. W. R. Ketterhagen, J. S. Curtis, C. R. Wassgren, and B. C. Hancock, "Predicting the Flow Mode from Hoppers Using the Discrete Element Method," *Powder technology* 195, no. 1 (2009): 1–10, https://doi.org/10.1016/j.powtec.2009.05.002.

50. A. Drescher, "Some Aspects of Flow in Granular Materials in Hoppers," *Philosophical Transactions of the Royal Society of London, Series A: Mathematical, Physical and Engineering Sciences* 356, no. 1747 (1998): 2649–2666.

51. R. H. Sabersky, C. E. Brennen, and T. V. Nguyen, "Funnel Flow in Hoppers," *Journal of Applied Mechanics* 47, no. 4 (1980): 729–735.

52. H. Ahn, Z. Başaranoğlu, M. Yılmaz, A. Buğutekin, and M. Z. Gül, "Experimental Investigation of Granular Flow through an Orifice," *Powder Technology* 186, no. 1 (2008): 65–71, https://doi.org/10.1016/j.powtec.2007.11.001.

53. D. Schulze, "Silo Design for Flow," in *Powders and Bulk Solids* (Springer International Publishing, 2021), 367–411, https://doi.org/10.1007/978-3-030-76720-4_10.

54. X. Huang, Q. Zheng, D. Liu, A. Yu, and W. Yan, "Hopper Shape Optimization for Improved Mass Flow," *Chemical Engineering Science* 253 (2022): 117579, https://doi.org/10.1016/j.ces.2022.117579.

55. W. A. Beverloo, H. A. Leniger, and J. Van de Velde, "The Flow of Granular Solids through Orifices," *Chemical engineering science* 15, no. 3-4 (1961): 260–269.

56. K. To, P. Y. Lai, and H. K. Pak, "Jamming of Granular Flow in a Two-dimensional Hopper," *Physical Review Letters* 86 (2001): 71–74, https://doi.org/10.1103/PhysRevLett.86.71.

57. F. Alonso-Marroquin and P. Mora, "Beverloo Law for Hopper Flow Derived from Self-similar Profiles," *Granular Matter* 23, no. 1 (2021): 7, https://doi.org/10.1007/s10035-020-01067-1.

58. P. A. Cundall and O. D. L. Strack, "A Discrete Numerical Model for Granular Assemblies," *Géotechnique* 29 (1979): 47–65.

59. Ansys, Rocky DEM Technical Manual, Ansys Inc., 2023.

60. E. A. Castañeda, R. P. León, and J. Cornejo, "FEM and DEM Simulations of Tire-Soil and Drill-Soil Interactions in off-Road Conditions for Mechanical Design Validation of a Space Exploration Rover," in 2021 12th International Conference on Mechanical and Aerospace Engineering (ICMAE) (2021).

61. M. A. El-Emam, L. Zhou, W. Shi, C. Han, L. Bai, and R. Agarwal, "Theories and Applications of CFD–DEM Coupling Approach for Granular Flow: A Review," *Archives of Computational Methods in Engineering* 28, no. 7 (2021): 4979–5020, https://doi.org/10.1007/s11831-021-09568-9.

62. A. Anandarajah, "Discrete-element Method for Simulating Cohesive Soil Behavior," *Journal of Geotechnical Engineering* 120 (1994): 1593–1613.

63. A. Hasan and K. A. Alshibli, "Discrete Element Modeling of Strength Properties of Johnson Space Center (JSC-1A) Lunar Regolith Simulant," *Journal of Aerospace Engineering* 23 (2010): 157–165, https://doi.org/10.1061/(ASCE)AS.1943-5525.0000020.

64. X. Sun, R. Zhang, X. Li, M. Zou, and H. Zhang, "Calibration of Simulation Parameters for in-situ Excavation of Lunar Highland Simulant," *Powder Technology* 471 (2026): 122070.

65. T. Matsushima, J. Katagiri, K. Uesugi, A. Tsuchiyama, and T. Nakano, "3D shape Characterization and DEM Simulation of Lunar Soil Simulant FJS-1," *Journal of Aerospace Engineering* 22 (2009): 15–23, https://doi.org/10.1061/ASCE0893-1321200922:115.

66. T. Liu, C. Wei, L. Liang, J. Zhang, and Y. Zhao, "Simulation and Analysis of the Lunar Regolith Sampling Process Based on the Discrete Element Method," *Transactions of the Japan Society for Aeronautical and Space Sciences* 57, no. 6 (2014): 309–316.

67. M. Jiang, Z. Shen, and S. Utili, "DEM Modeling of Cantilever Retaining Excavations," *Engineering Computations* 33 (2016): 366–394, https://doi.org/10.1108/EC-06-2014-0140.

68. O. R. Walton and R. L. Braun, "Viscosity, Granular-temperature, and Stress Calculations for Shearing Assemblies of Inelastic, Frictional Disks," *Journal of rheology* 30, no. 5 (1986): 949–980.

69. C. B. Fonte, J. A. Oliveira Jr, and L. C. de Almeida, "DEM-CFD Coupling: Mathematical Modelling and Case Studies Using ROCKY-DEM® and ANSYS Fluent®," in Proceedings of the 11th International Conference on CFD in the Minerals and Process Industries, Melbourne (CSIRO, 2015).

70. S. R. Schwartz, D. C. Richardson, and P. Michel, "An Implementation of the Soft-sphere Discrete Element Method in a High-performance Parallel Gravity Tree-code," *Granular Matter* 14, no. 3 (2012): 363–380, https://doi.org/10.1007/s10035-012-0346-z.

71. K. A. Alshibli and A. Hasan, "Strength Properties of JSC-1A Lunar Regolith Simulant," *Journal of Geotechnical and Geoenvironmental Engi-*

neering 135 (2009): 673–679, https://doi.org/10.1061/ASCEGT.1943-5606.0000068.

72. M. Paulick, M. Morgeneyer, and A. Kwade, "Influence of Elastic Particle Properties on DEM Simulation Results," *Powder Technology* 283 (2015): 66–76, https://doi.org/10.1016/j.powtec.2015.03.040.

73. J. Gong, X. Pang, Y. Tang, M. Liu, J. Jiang, and X. Ou, "Effects of Particle Shape, Physical Properties and Particle Size Distribution on the Small-strain Stiffness of Granular Materials: A DEM Study," *Computers and Geotechnics* (2024): 105903, https://doi.org/10.1016/j.compgeo.2023.105903.

74. J. K. Mitchell, W. N. Houston, R. F. Scott, N. C. Costes, W. D. Carrier, and L. G. Bromwell, "Mechanical Properties of Lunar Soil," *Proceedings of the Lunar Science Conference* 3 (1972): 3235–3253.

75. C. Ding, S. Xiong, J. Li, Y. Su, and S. Huang, "Yutu-2 Radar Observation of the Lunar Regolith Heterogeneity at the Chang'E-4 Landing Site," *Astronomy and Astrophysics* (2022): A43, https://doi.org/10.1051/0004-6361/202142803.

76. W. D. Carrier, G. R. Olhoeft, and W. Mendell, *Physical Properties of the Lunar Surface, Lunar Sourcebook* (Cambridge University Press, 1991), 475–594.

77. O. R. Walton, C. P. De Moor, and K. S. Gill, "Effects of Gravity on Cohesive Behavior of Fine Powders," *Granular Matter* 9 (2007): 353–363, https://doi.org/10.1007/s10035-006-0029-8.

78. J. Long-Fox, M. P. Lucas, Z. Landsman, C. Millwater, D. Britt, and C. Neal, "Applicability of Simulants in Developing Lunar Systems and Infrastructure: Geotechnical Measurements of Lunar Highlands Simulant LHS-1," In *Earth and Space*. (2022), 76–85, https://doi.org/10.1061/9780784484470.007.

79. I. Håkansson and J. Lipiec, "Usefulness of Relative Bulk Density Values in Soil Compaction Studies," *Soil and Tillage Research* 53, no. 2 (2000): 71–85, https://doi.org/10.1016/S0167-1987(99)00095-1.

80. Exolith Lab, "LHS-1 Lunar Highlands Simulant Fact Sheet," December 2023. [Online]. [Accessed 5 July 2024].

81. J. E. Colwell, S. Batiste, M. Horányi, S. Robertson, and S. Sture, "Lunar Surface: Dust Dynamics and Regolith Mechanics," *Reviews of Geophysics* 45, no. 2 (2007): 1–26, https://doi.org/10.1029/2005RG000184, Paper number 2005RG000184.

82. W. L. Zou, Y. L. Li, L. Chen, J. F. Zhang, and X. Q. Wang, "Mechanical Properties of QH-E Lunar Soil Simulant at Low Confining Stresses," *Journal of Aerospace Engineering* 29, no. 2 (2016): 04015036, https://doi.org/10.1061/(ASCE)AS.1943-5525.0000526.

83. J. Nie, S. Wang, Y. Cui, et al., "Analyzing the Mechanical Heterogeneity of the Chang'e-5 Lunar Breccia Clast: Implications for the Elastic Modulus of Lunar Rock," *Journal of Geophysical Research: Planets* 130, no. 6 (2025): e2024JE008849, https://doi.org/10.1029/2024EJ008849.

84. K. Yin, Z. Cheng, J. Liu, and A. Chen, "Shear Properties of LHS-1 and LMS-1 Lunar Regolith Simulants," *Planetary and Space Science* 226 (2023): 105630, https://doi.org/10.1016/j.pss.2022.105630.

85. A. Garcimartín, I. Zuriguel, A. Janda, and D. Maza, "Fluctuations of Grains inside a Discharging Two-dimensional Silo," *Physical Review E—Statistical, Nonlinear, and Soft Matter Physics* 84, no. 3 (2011): 031309, https://doi.org/10.1103/PhysRevE.84.031309.

86. I. Zuriguel, D. R. Parisi, R. C. Hidalgo, et al., "Clogging Transition of Many-particle Systems Flowing through Bottlenecks," *Scientific reports* 4, no. 1 (2014): 7324, https://doi.org/10.1038/srep07324.

87. K. T. Chau, R. H. C. Wong, and J. J. Wu, "Coefficient of Restitution and Rotational Motions of Rockfall Impacts," *International Journal of Rock Mechanics and Mining Sciences* 39, no. 1 (2002): 69–77, https://doi.org/10.1016/S1365-1609(02)00016-3.

88. J. Zhu, M. Zou, Y. Liu, K. Gao, B. Su, and Y. Qi, "Measurement and Calibration of DEM Parameters of Lunar Soil Simulant," *Acta Astronautica* 191 (2022): 169–177, https://doi.org/10.1016/j.actaastro.2021.11.009.

89. E. J. Garboczi, "Three-dimensional Shape Analysis of JSC-1A Simulated Lunar Regolith Particles," *Powder Technology* 207 (2011): 1–3, https://doi.org/10.1016/j.powtec.2010.10.014.

90. J. E. Lane, P. T. Metzger, and R. A. Wilkinson, "*A review of discrete element method (DEM) particle shapes and size distributions for lunar soil*," NASA/TM—2010-216257, Glenn Research Center Cleveland (2010).

91. A. A. Mirghasemi, L. Rothenburg, and E. L. Matyas, "Influence of Particle Shape on Engineering Properties of Assemblies of Two-dimensional Polygon-shaped Particles," *Geotechnique* 52, no. 3 (2002): 209–217, https://doi.org/10.1680/geot.2002.52.3.209.

92. N. Govender, D. N. Wilke, C. Y. Wu, R. Rajamani, J. Khinast, and B. J. Glasser, "Large-scale GPU Based DEM Modeling of Mixing Using Irregularly Shaped Particles," *Advanced Powder Technology* 29, no. 10 (2018): 2476–2490, https://doi.org/10.1016/j.apt.2018.06.028.

93. A. Shackelford, K. D. Hanna, M. Horton, and D. Noce, "Morphological and Spectral Characterization of Lunar Regolith Breakdown due to Water Ice," *The Planetary Science Journal* 5 (2024): 1–18, https://doi.org/10.3847/PSJ/ad0041.

94. P. A. Liever and J. West, "Particle Interaction Physics Model Formulation for Plume-surface Erosion," *AIAA SciTech Forum Proceedings* (2022), https://doi.org/10.2514/6.2022-2317.

95. K. J. Berger and C. M. Hrenya, "Predicting Regolith Erosion during a Lunar Landing," *Journal of Aerospace Engineering* 30 (2017): 04017027, https://doi.org/10.1061/(ASCE)AS.1943-5525.0000735.

96. A. Bajpai, A. Bhateja, and R. Kumar, "Plume-surface Interaction during Lunar Landing Using DSMC-DEM Coupling," *Physical Review Fluids* 9 (2024): 024306, https://doi.org/10.1103/PhysRevFluids.9.024306.

97. J. M. Long-Fox, Z. A. Landsman, P. B. Easter, C. A. Millwater, and D. T. Britt, "Geomechanical Properties of Lunar Regolith Simulants LHS-1 and LMS-1," *Advances in Space Research* 71 (2023): 5400–5412, https://doi.org/10.1016/j.asr.2023.02.034.

98. D. Rickman, C. Immer, P. Metzger, E. Dixon, M. Pendleton, and J. Edmunson, "Particle Shape in Simulants of the Lunar Regolith," *Journal of Sedimentary Research* 82, no. 11 (2012): 823–832, https://doi.org/10.2110/jsr.2012.69.

99. C. M. Pieters and S. K. Noble, "Space Weathering on Airless Bodies," *Journal of Geophysical Research: Planets* 121, no. 10 (2016): 1865–1884, https://doi.org/10.1002/2016JE005128.

100. S. Yu, J. Shang, Y. Chen, et al., "Power Spectra of Velocity Fluctuations in Granular Heap Flow," *Physical Review Letters* 135, no. 11 (2025): 118201, https://doi.org/10.1103/c2w1-wjq6.

101. T. Hwa and M. Kardar, "Avalanches, Hydrodynamics, and Discharge Events in Models of Sandpiles," *Physical Review A* 45, no. 10 (1992): 7002, https://doi.org/10.1103/PhysRevA.45.7002.

102. C. R. Wassgren, M. L. Hunt, P. Freese, J. Palamara, and C. Brennen, "Effects of Vertical Vibration on Hopper Flows of Granular Material," *Physics of Fluids* 14 (2002): 3439–3448, https://doi.org/10.1063/1.1503354.

103. A. Suzuki, H. Takahashi, and T. Tanaka, "Behavior of a Particle Bed in the Field of Vibration II, Flow of Particles through Slits in the Bottom of a Vibrating Vessel," *Powder Technology* 2, no. 2 (1968): 72–77, https://doi.org/10.1016/0032-5910(68)80040-3.

104. W. Schellart, "Shear Test Results for Cohesion and Friction Coefficients for Different Granular Materials, Scaling Implications for Their Usage in Analogue Modelling," *Tectonophysics* 324 (2000): 1–4, https://doi.org/10.1016/S0040-1951(00)00111-6.

105. B. A. C. S. Jayathilake, I. M. S. K. Ilankoon, and M. N. P. Dushyantha, "Assessment of Significant Geotechnical Parameters for Lunar Regolith Excavations," *Acta Astronautica* 196 (2022): 107–122, https://doi.org/10.1016/j.actaastro.2022.04.008.

106. F. Melo, P. Umbanhowar, and H. L. Swinney, "Transition to Parametric Wave Patterns in a Vertically Oscillated Granular Layer," *Physical Review Letter* 72 (1994): 172–175, https://doi.org/10.1103/PhysRevLett.72.172.

107. C. Bizon, M. D. Shattuck, J. B. Swift, W. D. McCormick, and H. L. Swinney, "Patterns in 3D Vertically Oscillated Granular Layers: Simulation and Experiment," *Physical Review Letter* 80 (1998): 57–60, https://doi.org/10.1103/PhysRevLett.80.57.

108. J. Yang and C. Daraio, "Frequency- and Amplitude-dependent Transmission of Stress Waves in Curved One-dimensional Granular Crystals Composed of Diatomic Particles," *Experimental Mechanics* 53 (2013): 469–483, https://doi.org/10.1007/s11340-012-9652-y.

109. B. Świtała, D. Leśniewska, and M. A. Kalwar, "Micro-mechanisms of Force Network Rearrangement in Granular Materials," *Computers and Geotechnics* 174 (2024): 106602, https://doi.org/10.1016/j.compgeo.2024.106602.

110. H. Li, J. Li, H. Fei, G. Hong, J. Dong, and A. Yu, "Chaotic Dynamics of Granules-beam Coupled Vibration, Route and Threshold," *Mechanical Systems and Signal Processing* 218 (2024): 111555, https://doi.org/10.1016/j.ymssp.2024.111555.

111. Y. Huang and H. Zheng, "Mechanical Characteristics of a Lunar Regolith Simulant at Low Confining Pressure," *Environmental Earth Sciences* 71 (2014): 3697–3703, https://doi.org/10.1007/s12665-013-2763-7.

112. S. Li, H. Zhang, J. Baeyens, M. Yang, Z. Li, and Y. Deng, "Vibro-fluidization of Cohesive Particles," *Powder Technology* 432 (2024): 119107, https://doi.org/10.1016/j.powtec.2023.119107.

113. O. R. Walton and S. M. Johnson, "DEM Simulations of the Effects of Particle Shape, Interparticle Cohesion, and Gravity on Rotating Drum Flows of Lunar regolith," (Earth and Space 2010: Engineering, Science, Construction, and Operations in Challenging Environments, 2010): 36–41, https://doi.org/10.1061/41096(366)5.

114. H. P. Zhang and H. A. Makse, "Jamming Transition in Emulsions and Granular Materials," *Physical Review E—Statistical, Nonlinear, and Soft Matter Physics* 72, no. 1 (2005): 011301, https://doi.org/10.1103/PhysRevE.72.011301.

115. Z. Ning and T. M. Evans, "Discrete Element Method Study of Shear Wave Propagation in Granular Soil," in *Proceedings of the 18th International Conference on Soil Mechanics and Geotechnical Engineering* (France, 2013), 1031–1034.